ILARIA AIMO

STUDIES ON MONOLITHIC ACTIVE PIXEL SENSORS FOR THE INNER TRACKING SYSTEM UPGRADE OF ALICE EXPERIMENT

DOTTORATO DI RICERCA IN FISICA

XXVII CICLO DI DOTTORATO

Supervisor: Prof. Michelangelo Agnello
Politecnico di Torino
Dipartimento di Scienza Applicata e Tecnologia

Torino, 12 Febbraio 2015

An expert is a man who has made all the mistakes which can be made, in a very narrow field.

Niels Bohr

CONTENTS

LIST OF FIGURES

LIST OF TABLES

INTRODUCTION

ALICE (A Large Ion Collider Experiment) is a general-purpose, heavy-ion detector at the CERN LHC. It is designed to study the physics of strongly interacting matter, and in particular the properties of the Quark-Gluon Plasma (QGP), using nucleus- nucleus collisions at unprecedented energy densities.

One of the major goals of the ALICE physics program is the study of rare probes at low transverse momentum. The reconstruction of the rare probes requires a precise determination of the primary and secondary vertices that is performed in ALICE by the Inner Tracking System (ITS). The present ITS made of 6 layers of three technologies of silicon devices allows, for example, to reconstruct D mesons with the transverse momentum down to $\sim 2\,GeV/c$.

In order to enhance the ALICE physics capabilities, and, in particular, the tracking performance for heavy-flavour detection, an upgrade of the ITS has been planned for the second long shutdown of LHC (LS2) in 2017/18.

The upgraded detector will have greatly improved features in terms of impact parameter resolution, standalone tracking efficiency at low p_T , momentum resolution and readout capabilities.

Monolithic Active Pixel Sensors (MAPS) can offer a granularity 50 times larger than in current ITS and also significantly reduce the material budget. Therefore, MAPS were chosen to be implemented in all layers of the new ITS.

In the present work the characteristics of MAPS prototypes in the ALICE upgrade framework were studied, including noise performances, response to soft X-rays emitted by ^{55}Fe source, signal to noise ratio, detection efficiency and spatial resolution.

Morever a development of a testbeam telescope setup designed to perform a comparative study of the first two full scale MAPS prototypes designed for the ALICE ITS will be discussed.

The schema of the chapters is as follows.

IN THE FIRST CHAPTER a brief overview of the ALICE physics motivations will be given.

IN THE SECOND CHAPTER the main sub-systems of the ALICE experiment, their performance and the dedicated offline analysis framework will be presented.

IN THE THIRD CHAPTER the limitations of the current apparatus, the physics motivations for the ITS upgrade and its main specifications will be described.

THE FOURTH CHAPTER will describe the main features of the Monolithic Active Pixels Sensors, focusing in particular on the ALICE ITS MAPS developments.

IN THE FIFTH CHAPTER the characterization results on MIMOSA32, one of the first MAPS prototypes developed within the ALICE framework, will be illustrated.

THE SIXTH CHAPTER will illustrate the testbeam characterization results on MIMOSA22ThrB prototype obtained with a testbeam telescope under development at the Laboratori Nazionali di Frascati.

1 ALICE PHYSICS MOTIVATIONS

Contents

The goal of heavy-ion collisions is to study the properties of nuclear matter under extreme conditions of density and temperature. Quantum Chromo-Dynamics (QCD), the theory which describes strong interactions, predicts that nuclear matter in these conditions could undergo a transition toward a state of matter called Quark-Gluon Plasma (QGP) in which quarks and gluons are deconfined [1].

Recent calculations of Lattice QCD predict that the critical temperature at which the phase transition occurs is $T_c \simeq 160\,MeV$ and corresponds to an energy density of the nuclear matter of $\epsilon_c \simeq 0.7\,GeV/fm^3$ [2].

The first indications of the creation of a deconfined state of matter were found at the Super Proton Synchrotron (SPS) at CERN colliding lead nuclei at $\sqrt{s_{NN}} = 17.2\,GeV$. Further studies were then performed at the Relativistic Heavy-Ion Collider (RHIC) colliding gold and copper ions at $\sqrt{s_{NN}} = 200\,GeV$. The last remarkable step towards a deeper understanding of the physics of the QGP was done at CERN in 2010 when the Large Hadron Collider (LHC) started to collide lead nuclei at $\sqrt{s_{NN}} = 2.76\,TeV$.

In this Chapter, the basic features of QCD will be presented in order to introduce the physics motivations at the basis of the ALICE experiment.

1.1 THE QUANTUM CHROMODYNAMICS

The *Quantum Chromo-Dynamics* (QCD) is the gauge field theory which describes the features of the interaction between the quarks and gluons found in hadrons in the Standard Model [3].

This gauge theory is based on the symmetry group $SU(3)$ and characterized by the lagrangian density:

$$\mathcal{L} = -\frac{1}{4}F^a_{\mu\nu}F^{\mu\nu}_a + i\sum_q \bar{\psi}^i_q \gamma^\mu (D_\mu)_{ij} \psi^j_q - \sum_q m_q \bar{\psi}^i_q \psi_{q\,i} \qquad (1)$$

where, the non-Abelian gluon field strength tensor $F^a_{\mu\nu}$ has the form:

$$F^a_{\mu\nu} = \partial_\mu A^a_\nu - \partial_\nu A^a_\mu + g f_{abc} A^b_\mu A^c_\nu \qquad (2)$$

and the covariant derivative D_μ:

$$(D_\mu)_{ij} = \partial_\mu \delta_{ij} - i g_s \left(\frac{\lambda_a}{2}\right)_{ij} A^a_\mu \qquad (3)$$

λ_a are the eight $SU(3)$ group generator (3×3 matrices), f_{abc} are the group structure constants and g_s is the gauge coupling constant.

A^a_μ are massless vector bosons (no mass term is present in the QCD lagrangian) interacting with quarks via the vertex represented in Fig. 1a and among themselves via those represented in Fig. 1b and 1c. These last vertexes are characteristics of non abelian theories such as QCD.

For a general discussion of the QCD see [4].

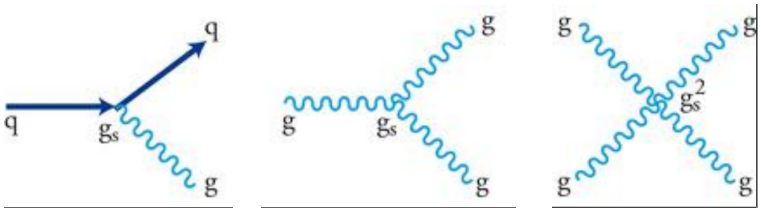

(a) Quark-Gluons interaction.

(b) Gluon gluon interaction.

(c) Gluon gluon interaction.

Figure 1: Interaction vertexes in QCD.

1.2 RUNNING COUPLING CONSTANT

The QCD coupling constant α_s is related to the scale of the transfered momentum q by the relation:

$$\alpha_s(|q^2|) = \frac{\alpha_0}{1 + \alpha_0 \frac{33-2n_f}{12\pi} \ln \frac{|q^2|}{\mu^2}} \qquad (4)$$

where α_0 is the strong coupling constant for transfered momentum μ and n_f is the number of quark flavours [5].

This running shows two energetic ranges:

- For $|q^2| \to \infty$, $\alpha_s(|q^2|) \to 0$. *Asymptotic freedom*. In very high-energy reactions (i.e. on short space-time scales) quarks and gluons interact very weakly. This means that in high-energy interactions quarks and gluons can be considered as free particles.
- For $|q^2| \to 0$, $\alpha_s(|q^2|) \to \infty$. *Confinement*. The force between quarks does not diminish as they are separated. Because of this, it would take an infinite amount of energy to separate two quarks; they are bound into hadrons such as the proton and the neutron.

1.3 PHASE TRANSITION AND QGP

Several models, using the QCD theory as a starting point, predict that hadronic matter, in conditions of extreme energy density and temperature, could undergo a phase transition to a state of matter where quarks and gluons are deconfined. The deconfined state is called *quark-gluon Plasma* [6] and is described as matter which no longer consists of hadrons (protons, neutrons) but it is made of their fundamental constituents, the quarks and the gluons.

The verification of the existence of the QGP state is also of cosmological and astrophysical interest because it is expected that the QGP was the state of matter in the first instants ($t < 10^{-6}$ s) of the Universe after the Big-Bang. Moreover, a plasma of quarks and gluons at low temperature with high baryon density could be present in the core of neutron stars.

The confinement property is not expected to be true in extreme conditions. Non-perturbative QCD calculations predict that at baryon densities larger than $\sim 5-10$ times the density of the ordinary nuclear matter ($\rho_0 = 0.15$ nucleons/fm^3) or at temperatures of the order of $140-200$ MeV, nuclear matter should undergo a phase transition into the QGP state.

There are two crucial quantities used to describe the phase diagram of the nuclear matter: *temperature* and *Baryon-chemical potential* [1].

In Fig. 2 a qualitative view of the QCD phase space diagram is presented where μ_B is replaced by the net baryon density (directly proportional to μ_B). It is possible to notice notice that for low values of Baryon-chemical density and for low temperatures the ordinary nuclear matter is present. If the nuclear matter is compressed (i.e.

1 In statistical mechanics, the chemical potential is the minimal energy necessary to add (or extract) a particle to a system: $\mu = dE/dN$. The Baryon-chemical potential is directly proportional to the baryon-number density.

increasing μ_B) or heated up (i.e. increasing T) nucleons interact and form pions and excited states of protons and neutrons (Δ resonances) which can reach the thermal equilibrium. This state of hadronic matter is called *hadron gas*.

The phase transition line separates the phase space into two regions: above this line conditions are typical of quark-gluon Plasma phase, below this line hadron gas is expected.

The critical point (μ_{B_c}, T_c) separates the first order phase transition and the crossover region.

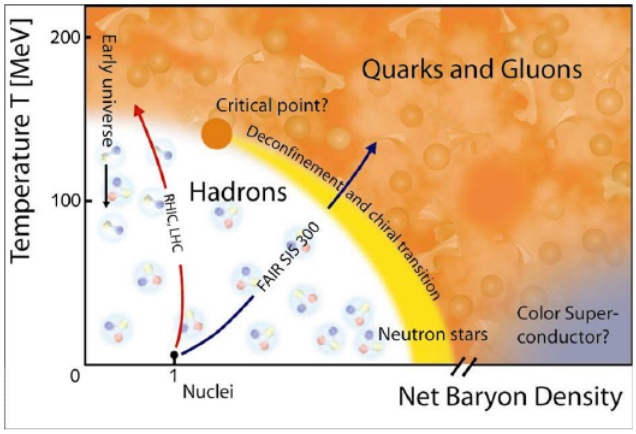

Figure 2: Qualitative view of the QCD phase space diagram

1.4 QGP PREDICTIONS

The description of microscopic processes involving quarks and gluons can be done by means of three categories of theoretical tools :

- *Perturbative QCD (pQCD)*, allows us to use a perturbative expansion in series of the strong coupling constant α_s with the requirement that $\alpha_s \ll 1$. Therefore, pQCD can be used only to describe those processes which guarantee such condition, i.e. processes with large $|q^2|$, for example heavy flavour production in hadron collisions.

- *Lattice QCD*: is a non perturbative treatment of quantum chromodynamics formulated on a discrete lattice of space-time coordinates which provides a quantitative understanding of the new phase of matter [7].

  Lattice QCD calculations can reproduce some of the pQCD results and, in addition, provide a description of non-perturbative processes. Nevertheless, lattice QCD calculations show uncertainties related to limitations on the lattice spacing and on the

size of the lattice partly due to the high computing power required by this numerical approach.

- *Effective models*, these models are based on QCD and provide a phenomenological description of the physical processes.

  This approach is extremely useful to predict some of the fundamental properties of the hadronic matter.

  The MIT bag model [8], the Nambu-Jona-Lasinio (NJL) model [9] and the parton model are among the effective models largely used for practical calculations.

1.5 HEAVY ION COLLISIONS

To explore experimentally the possible existence of the QGP, it is mandatory to create a strongly interacting system which satisfies some requirements:

- in order to use macroscopic variables the system has to be extended in space (i.e. a big number of interacting nucleons is needed). The space scale of the system has to be larger than the typical scale of strong interaction ($\sim 1\,\mathrm{fm}$);
- the system must be long lived: in order to describe the system using thermodynamics the system must reach thermal equilibrium ($\tau > 1\,\mathrm{fm\,c^{-1}}$);
- the system must be composed of strong interacting matter (i.e. quarks and gluons).

Nucleus–nucleus collisions can satisfy all these demanding requirements. Indeed, high energy nucleus-nucleus collisions create nuclear matter in conditions of extreme temperature and density, as the kinetic energy lost by the incident projectiles is deposited in the large volume of nuclear matter involved in the reaction.

The first experiments have been performed with fixed target configuration at the Alternating Gradient Synchrotron (AGS) in Brookhaven and the Super Proton Synchrotron (SPS) at CERN, with centre of mass (CM) energies in the range between $2\,AGeV$ and $18\,AGeV$ (A is the number of nucleons in the nucleus). Later experiments with colliding nuclear beams commenced at RHIC in Brookhaven, taking advantage of the higher energy of $200\,AGeV$ available in the CM frame; the highest energy has been reached at the Large Hadron Collider (LHC) at CERN in 2010, this time with a CM energy of $2760\,AGeV$.

The system created in a $Pb-Pb$ collision can reach a volume of the order of $1000\,\mathrm{fm^3}$, consisting of ~ 1000 hadrons and, already at SPS energies, can reach an energy density ~ 200 times larger than in a nucleus ($0.15\,\mathrm{GeV/fm^3}$).

1.5.1 Collision geometry

The Glauber model [10] provides a phenomenological description of the nucleus-nucleus collision starting from the geometrical configurations of the colliding nuclei. This model describes the nucleus-nucleus interaction in terms of interactions between the constituent nucleons.

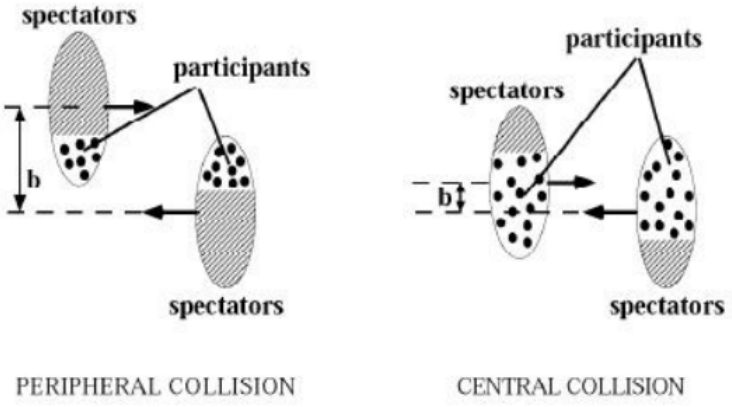

Figure 3: Geometry of the collision between two nuclei.

In Fig. 3 the collision of two nuclei is schematically represented as seen in the axis beam direction (z axis), the shape of the nuclei is depicted as a prolate sphere in order to take into account the relativistic lenght contraction .

The *impact parameter* b is a crucial quantity. It measures the distance between the centres of two nuclei, separating nucleons into *participants*, which suffer at least one collision with a nucleon of the other nucleus, and *spectators* which proceed with little perturbation along the original direction. In a central collision the impact parameter is close to zero and the two nuclei completely overlap.

The Glauber model allows for a simple calculation of the number of nucleons involved in a collision occuring with a given value of b.

From this model one obtains the number of participant nucleons N_{part}, i.e. the number of nucleons that experience at least one interaction, and the number of collisions N_{coll}.

This offers a way of indirectly measuring the impact parameter of the collision by the detection of the nucleons that have not interacted, i.e. the spectators; in heavy ions experiment this is done by putting calorimeters close to the beam line thus detecting those nucleons that proceed on their straight path.

The impact parameter allows to classify the collisions in class of *centrality*. The smaller is the impact parameter the more participant nucleons are involved in the collision and, consequently, the centrality of the collision increases. It is important to distinguish between

central and peripheral collisions, because the energy density released is maximal in a central collision. In this case, when the two nuclei collide a large volume of hot hadronic matter is created possibly fulfilling the conditions for QGP formation.

1.5.2 Collision evolution

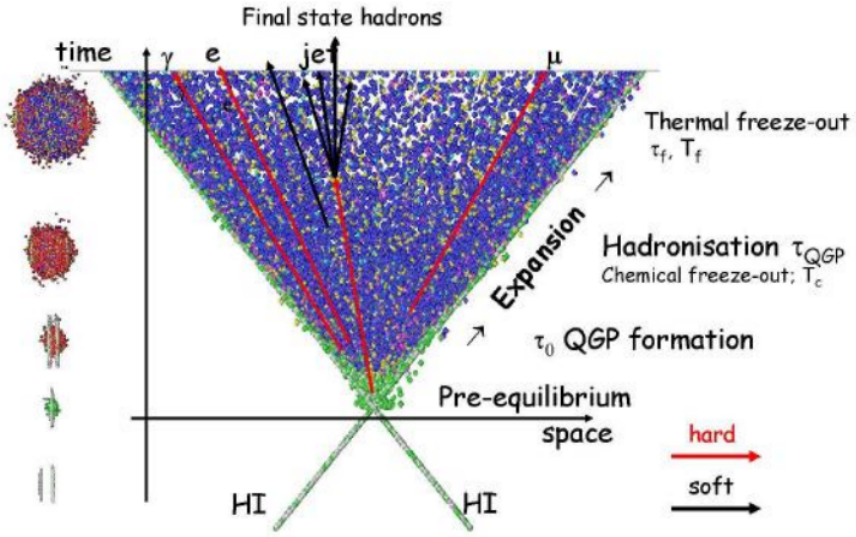

Figure 4: Space-time evolution of a central collision.

Before the collision, the two interacting nuclei can be represented by two thin disks, in order to take into account the Lorentz contraction (Fig. 4). The projectile nucleus travels along the beam axis (z) with a velocity close to the speed of the light and collides with the target nucleus, coming in the opposite direction [11].

A large amount of inelastic scatterings, among the nucleons of the two colliding nuclei, are then expected to take place. In each inelastic collision, the nucleons involved in the process lose energy and momentum. At the LHC energies, the nucleons involved in the interactions still have enough energy to move forward from the interaction region and thus the system created in the collision is characterized by a large energy density but a small net baryon content (*transparency*).

If the system is sufficiently interacting, it reaches the thermal equilibrium at a proper time τ_0 after the so called *formation phase* or *pre-equilibrium* (See Fig. 4), after that the system expands rapidly and cools down experiencing characteristics stages during the evolution, which are:

- *QGP formation* (τ_0) is when equilibrium is reached among the partonic constituents of the system;

- *hadronization* when partons fragment into colourless hadrons;
- *chemical freeze-out* (τ_c) is when inelastic interaction among constituents cease;
- *thermal freeze-out* (τ_f) is when elastic interaction among constituents cease.

After the equilibrium is reached, the system expands in a collective flow during the deconfined phase and the hadronization process. When inelastic interactions between hadrons cease and particle multiplicities reach their final configuration, the so called chemical freeze-out is reached (τ_c). When even elastic collisions stop, thermal freeze-out τ_f , hadrons stream freely away to be detected by the experiment.

The short life time of the QGP (only 10^{-23} s), together with the impossibility to detect free quarks, does not allow to measure the phase transition directly. For this reason, observables that can probe the possible formation of the QGP are mainly indirect signals which should be able to test the properties of the medium at different stages of the collision evolution.

In the following, the most representative phenomena as observable probes (hard and soft) of the Quark-Gluon Plasma are described and the most relevant experimental results obtained in nuclear experiments are listed.

1.5.3 Particle multiplicity

The main observables used to characterize the multiplicity of produced particle are the rapidity and the pseudo-rapidity density distributions of primary charged particles. The pseudo-rapidity η is referred to the polar angle θ with respect to the beam axis with which a particle is emitted from the interaction vertex. The pseudo-rapidity can be expressed as

$$\eta = -\ln \tan \frac{\theta}{2} = \frac{1}{2} \ln \frac{|p| + p_z}{|p| - p_z} \tag{5}$$

where p and p_z are the total momentum and longitudinal momentum of the emitted particle respectively. The rapidity y, instead, is given by:

$$y = \frac{1}{2} \ln \frac{E + p_z}{E - p_z} \tag{6}$$

Generally it is easier to measure η than y since the pseudo-rapidity does not require particle identification.

The left panel of Fig. 5 shows the dependence of $dN_{ch}/d\eta/(0.5\langle N_{part}\rangle)$ as a function of N_{part} measured with ALICE: the charged-particle

density per participant pair increases with centrality from 4.4 ± 0.4 for most peripheral to 8.3 ± 0.3 for most central events. In the same plot, the results obtained at RHIC (averaged among all the experiments) are shown after being scaled by a factor 2.1. The centrality dependence of the two measurements is very similar [12].

In the right panel of Fig. 5, different measurements of the particle pseudorapidity density for central collisions normalized to the number of participant pairs are presented as a function of the centre-of-mass energy for different colliding systems [13]. It is interesting to observe that the energy dependence of the charged multiplicity for central heavy-ion collisions is steeper than for pp and $\bar{p}p$ collisions and exhibits a power-law scaling, which was confirmed by the ALICE, CMS and ATLAS measurements at the LHC in central Pb-Pb collisions at $\sqrt{s_{NN}} = 2.76\,TeV$ [13, 14, 15]. A strong increase, by a factor 2.2, in the pseudo-rapidity density is observed at the LHC if compared to the STAR results from Au-Au collisions at RHIC at $\sqrt{s_{NN}} = 200\,GeV$ [16].

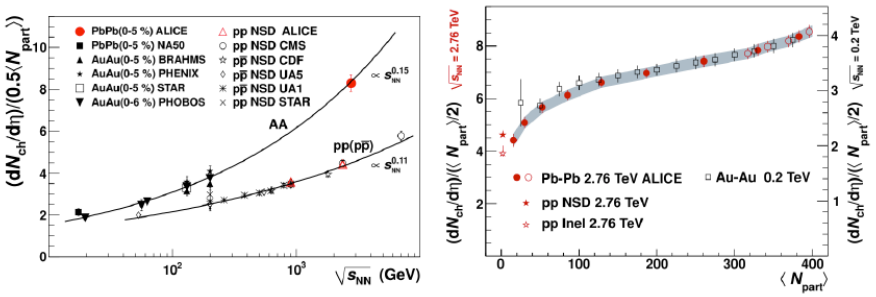

Figure 5: (Left) Charged particle pseudo-rapidity density per participant pair for central nucleus-nucleus collisions as a function of the centre-of-mass energy measured in different colliding systems [13]. (Right) Centrality dependence of $dN_{ch}/d\eta/(0.5\langle N_{part}\rangle)$ for Pb-Pb collisions at $\sqrt{s_{NN}} = 2.76\,TeV$ measured with ALICE and Au-Au collisions at $\sqrt{s_{NN}} = 0.2\,TeV$ obtained with an average of RHIC results. The latter measurement is scaled by a factor 2.1 [12].

The rapidity distribution of these produced particles could then be used to estimate the initial energy density in the central reaction zone through the Bjorken equation [11]:

$$\epsilon_{Bj} = \frac{m_t}{\tau_0 A} \frac{dN}{dy}\bigg|_{y=y_{CM}} \tag{7}$$

where A is the transverse overlapping area in the collision and m_t the mean transverse mass of the produced particles, τ_0 is the proper production time of the particles (which is energy dependent of the order of $1\,fm/c$).

Using Eq. (7) the energy density ϵ_{Bj} at mid-rapidity can be estimated. ALICE obtained for Pb-Pb collisions in the centrality range

$0-5\%$ $\epsilon_{Bj} \approx 16\,GeV/fm^3$, about a factor 3 larger than the corresponding one at RHIC in the same centrality range.

For both the estimations, the QGP formation time considered was $\tau_0 = 1fm/c$. The energy density measured at LHC and at RHIC is well above the critical density $\epsilon_c \sim 1GeV/fm^3$ expected for the phase transition according to lattice QCD calculations.

1.5.4 Particle spectra and radial flow

In heavy-ion collisions, most of the particles produced are hadrons generated in soft (non-perturbative) processes: these particles undergo the various phases of the system evolution up to the freeze-out. Particle spectra are relevant because they carry indirect information about the early stages of the collision. At a given beam energy in nucleus-nucleus collision, particle spectra can be reproduced by a model based on a superposition of local thermal motion and global collective expansion.

The shape of the spectrum of every hadronic specie i for low p_T values can be fitted with the following function:

$$\frac{dN_i}{m_T dm_T dy} \propto e^{-m_T/T_{slope_i}} \tag{8}$$

where m_T is the transverse mass, y is the particle rapidity and T_{slope_i} is a fit parameter. It has been observed that T_{slope_i} shows a linear dependence on the mass of the hadron. This dependence can be interpretated as follows:

$$T_{slope_i} = T_f + \frac{1}{2} m_i \langle v_\perp \rangle^2 \tag{9}$$

where T_f is the thermal freeze-out temperature, m_i is the hadron mass and $v_\perp$ is the surface velocity at freeze-out.

In Fig. 6, the p_T-distributions of pions, kaons and protons measured with ALICE in central Pb–Pb collisions at $\sqrt{s_{NN}} = 2.76\,TeV$ are shown [17] and compared to the results obtained at RHIC by the STAR [16] and PHENIX [18] collaborations in Au-Au collisions at $\sqrt{s_{NN}} = 200\,GeV$.

In the same figure, ALICE results are compared to the predictions of theoretical calculations based on a hydrodynamic approach [19, 20, 21].

The study of the spectra of identified particles, hence, can be used to separate the thermal component from the radial flow.

The temperature of thermal freeze-out and the surface velocity can be extracted from the distribution of transverse momentum spectra via Blast wave fits [22].

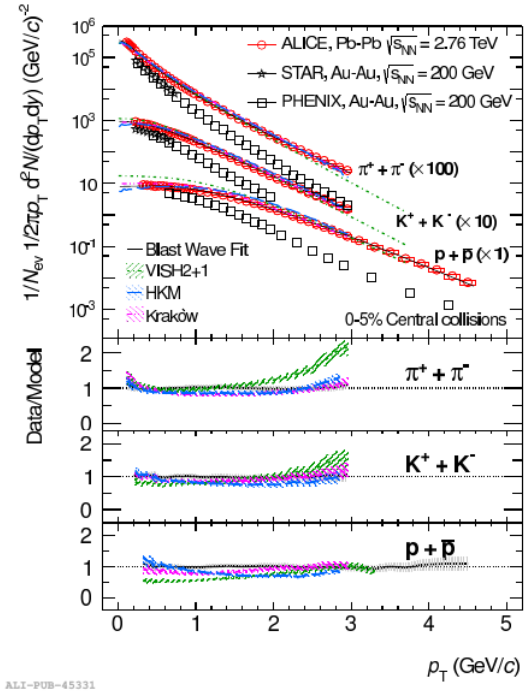

Figure 6: Particle spectra measured in central Pb–Pb collisions at $\sqrt{s_{NN}} = 2.76\,TeV$ by ALICE [17] compared to results obtained at RHIC in Au–Au collisions at $\sqrt{s_{NN}} = 200\,GeV$ [16, 18] and to the predictions of a hydrodynamical calculations [19, 20, 21]. The 5% most central collisions (see Sec. 1.5.1) are considered.

1.5.5 Elliptic flow

In non-central heavy ion collisions, an initially asymmetric overlap region is created. Due to pressure gradients, this almond shaped region tends to assume a more symmetric shape as the system expands. If the initially produced particles scatter enough in the overlap region, then the spatial anisotropy is converted into a momentum anisotropy which can be detected even much time after the thermal freeze-out.

The momentum anisotropies lead to a dependence of the transverse momentum distribution on the emission angle relative to the reaction plane, defined as the plane containing both the impact parameter vector and the longitudinal axis of the collision (Fig. 7). Expressing the azimuthal particle distributions relative to the reaction plane in Fourier series one gets [23]:

$$\frac{dN}{d(\phi - \Psi_{RP})} = \frac{N_0}{2\pi}\left\{1 + \sum_n 2v_n \cos\left[n(\phi - \Psi_{RP})\right]\right\} \qquad (10)$$

where N_0 is a normalized constant, ϕ and Ψ_{RP} are the azimuthal angles of the outgoing particles and of the reaction plane respectively.

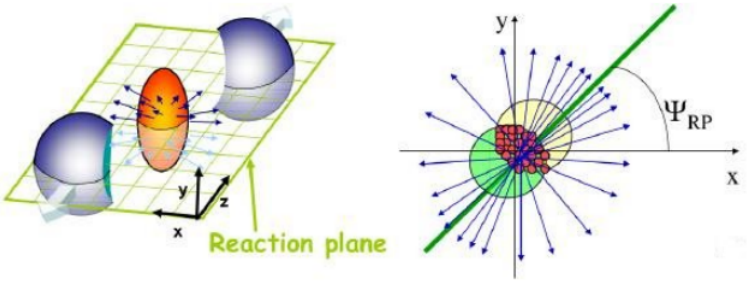

Figure 7: A non central heavy-ion collision showing how the reaction plane is defined

The first coefficient of the series, v_1, is called *directed flow*, while the second coefficient, v_2, is called *elliptic flow*.

A non zero v_1 implies a preferential direction in the emitted particles. A non zero v_2, which is expected to be the dominant armonic, indicates, instead, a different emission between the in-plane direction (parallel to the reaction plane, along the minor-axis of the ellipse in the overlap region) and the out-of-the-plane one.

The elliptic flow is specifically studied in order to test hydrodynamical models [24] which aim at describing the evolution of the system created in the collision as the evolution of a fluid. These models should be able to reproduce both radial and elliptic flow measured values.

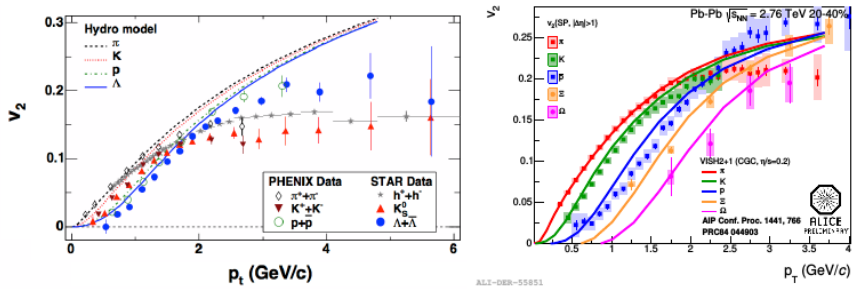

Figure 8: (Left) p_T-differential v_2 for identified π, K, p and Λ measured by STAR [25] and PHENIX [26] in semi-peripheral Au-Au collisions at $\sqrt{s_{NN}} = 200\,GeV$ compared to hydrodynamical calculations. (Right) v_2 of pions, kaons, protons, Λ, Ξ and Ω as a function of the transverse momentum measured by ALICE in Pb-Pb collisions in the centrality range $40-50\%$ [27] compared to hydrodynamic calculations [28].

In the left panel of Fig. 8 the p_T-differential v_2 measured by STAR and PHENIX experiments for different particle species are compared to hydrodynamical predictions. The model reproduces well RHIC measurements in the low-intermediate transverse momentum region. At higher p_T a hydrodynamic approach cannot be applied since high

p_T particles undergo few rescatterings with the medium and are not expected to reach the thermal equilibrium.

The ALICE experiment also measured elliptic flow in Pb-Pb collisions at $\sqrt{s_{NN}} = 2.7\,TeV$ in various centrality intervals [27]. In the right panel of Fig. 8 the v_2 of pions, kaons, protons, Λ, Ξ and Ω as a function of the transverse momentum are shown for events in the centrality range $40-50\%$ and compared to hydrodynamic calculations [28].

At LHC energies, the p_T-integrated elliptic flow increases by $\approx 30\%$ for semi-peripheral events with respect to RHIC measurements. In addition, it shows a stronger dependence on particle mass than at RHIC, with light and heavy particles pushed further apart from each other due to the increased radial flow.

1.5.6 Jet quenching

In hadronic collisions, hard parton scatterings occurring in the initial interaction produce cascades of consecutive emissions of partons, called jets. The jets fragment in hadrons during the hadronisation phase. The final state is characterized by clusters of particles close in the phase space. Their transverse momenta relative to the jet axis are small compared to the jet component along the jet axis and this collimation increases with increasing jet energy.

When traversing the QGP, partons are expected to lose an amount of energy which is proportional to the square of the in-medium path length causing therefore the so-called *jet quenching* effect when QGP is produced [29].

Some of the consequences of the "jet quenching" effect are:

- reduction of the high-p_T particle yield;
- depencence on the impact parameter of the collision: jet quenching is expected to be larger for central collisions;
- two back-to-back jets with high momentum are not likely to be reconstructed because jets with a longer path in the nuclear medium become softer and thus are not found by the jet reconstruction algorithm.

The phenomenon of jet quenching can be quantitatively estimated by measuring the *nuclear modification factor*, R_{AA} which is defined as:

$$R_{AA} = \frac{\left(\frac{dN}{dp_T}\right)_{AA}}{N_{coll} \cdot \left(\frac{dN}{dp_T}\right)_{NN}} \tag{11}$$

where $(dN/dp_T)_{AA}$ is the p_T-spectrum of particle produced in the nucleus-nucleus collision, $(dN/dp_T)_{NN}$ is the p_T spectrum from the

p-p collision and N_{coll} is the mean number of binary collisions between nucleons.

The R_{AA} value gives an information of what kind of collision we have because:

- hard processes are expected to scale with the number of binary collisions N_{coll}, hence without any nuclear effect $R_{AA} = 1$ is expected in the high-p_T region.
- soft processes are expected to scale with the number of participants, therefore for low-p_T hadron $R_{AA} < 1$ is expected.

This difference in the expected scaling of spectra is due to the difference in formation time of soft and hard hadrons, i.e. τ_f is smaller for hard hadrons than for the soft hadrons.

In collisions between nuclei possible nuclear effects could modify the expected shape; nuclear effects can be classified into initial state and final state effect.

INITIAL STATE EFFECTS :

- *Cronin effect*: it is due to the fact that before the hard scattering, partons could have several elastic scattering with partons of the target nucleus. In this way partons achieve a p_T distribution proportional to the square root of the number of elastic collisions, named *random walk*. The effect of these elastic interactions is to rise the p_T value of hadrons in the final state. For high-p_T hadrons this effect has to be sub-dominant.
- *Modification of the PDF*: PDFs inside the nuclei are different from the PDFs calculated for free nucleons.

FINAL STATE EFFECTS :

- *Energy loss - jet quenching*: in a hot and coloured medium partons lose energy interacting with the color field of the system, especially for radiative loss. This effect reduces the production of hard hadrons, and is a signal of the possible formation of a new state of matter.
- *Fragmentation and coalescence* are the fragmentation of a hard parton into soft hadrons and the recombination of two soft p_T partons creating a hadron with higher p_T respectively. The mechanism of hadronization in the medium could modify the p_T spectra of hadrons.

The value R_{AA} is expected to be:

- $R_{AA} \simeq 1$ for high-p_T hadrons or hadrons with heavy quarks if no nuclear effect is present;

- $R_{AA} > 1$ for intermediate p_T as consequence of the Cronin effect
- $R_{AA} < 1$ if a suppression of the hadron spectrum is present. This last scenario is what is expected to observe at high p_T in case of jet quenching.

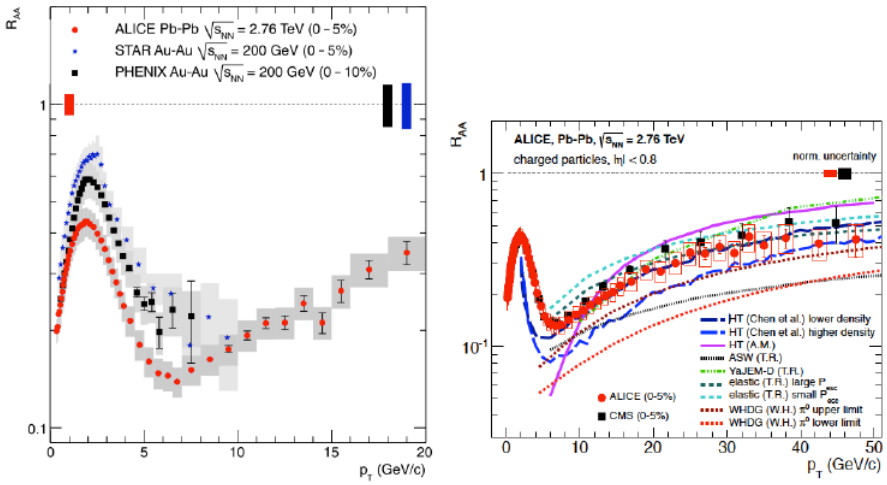

Figure 9: (Left) Nuclear modification factor of charged hadrons measured with ALICE in central Pb–Pb collisions at $\sqrt{s_{NN}} = 2.7\,TeV$ [30] compared to the results obtained by the STAR [31] and PHENIX [32] collaborations at RHIC in Au-Au collisions at $\sqrt{s_{NN}} = 200\,GeV$. (Right) Nuclear modification factor of charged hadrons measured with ALICE compared to the results obtained by the CMS collaboration [33] and to the predictions of theoretical calculations based on in-medium energy loss [30].

In the left panel of Fig. 9, the PHENIX results in the centrality range $0-10\%$ [32] and the STAR results in $0-5\%$ [31] are presented. In the same plot the R_{AA} of charged hadrons measured by ALICE in Pb-Pb collisions at $\sqrt{s_{NN}} = 2.7\,TeV$ in the centrality range $0-5\%$ is presented [30].

At $p_T \approx 1\,GeV/c$ the magnitude of the suppression measured with ALICE is similar to that observed at RHIC. In the intermediate p_T region, a strong dependence on p_T is observed with a maximum around $p_T = 2\,GeV/c$ for all the measurements. For $p_T = 6-7 GeV/c$, in which the effects of in-medium energy loss starts to be dominant, the ALICE result indicates a stronger suppression with respect to RHIC energies. This evidence suggests an enhanced energy loss at LHC that can be a consequence of the larger medium density. In addition, it can also indicates a more relevant fraction of high-p_T hadrons which originate from fragmentation of gluons that are expected to lose more energy with respects to quarks in radiative processes.

A comparison to the results obtained by the CMS collaboration in Pb-Pb collisions at $\sqrt{s_{NN}} = 2.76\,TeV$ [33] is presented in the right panel of Fig. 9 [30]: the CMS result is fully in agreement with the ALICE measurement within the uncertainties. In the same plot, the predictions of various theoretical calculations based on in-medium energy loss are superimposed.

The observed suppression of high-p_T particles in central Pb-Pb collisions provides evidence for strong parton energy loss and a large medium density at the LHC. In addition, the observed trend of the R_{AA} as a function of the transverse momentum suggests a relevant decrease of the relative energy loss with increasing p_T .

2 ALICE EXPERIMENT

Contents

2.1 AN OVERVIEW ON THE LARGE HADRON COLLIDER

The LHC is a two-ring machine installed in a 26.7 km long circular tunnel, lying about 100 m below the ground at the frontier between France and Switzerland.

The LHC was designed to deliver pp collisions at $\sqrt{s} = 14\,TeV$ and Pb-Pb collisions at $\sqrt{s_{NN}} = 5.5\,TeV$. The system which allows to accelerate protons and ions at these energies is extremely complex and benefits from the previous accelerator lines that were built in the last decades at CERN.

Protons are extracted from a hydrogen tank and injected in a linear accelerator (Linac2) in which they reach an energy of 50 MeV. After that, they are accelerated up to 1.4 GeV in the Proton Synchrotron Booster (PSB) and injected in the Proton Synchrotron (PS) which leads to the the Super Proton Synchrotron (SPS). After the SPS, protons at 450 GeV can be injected in the LHC accelerator ring.

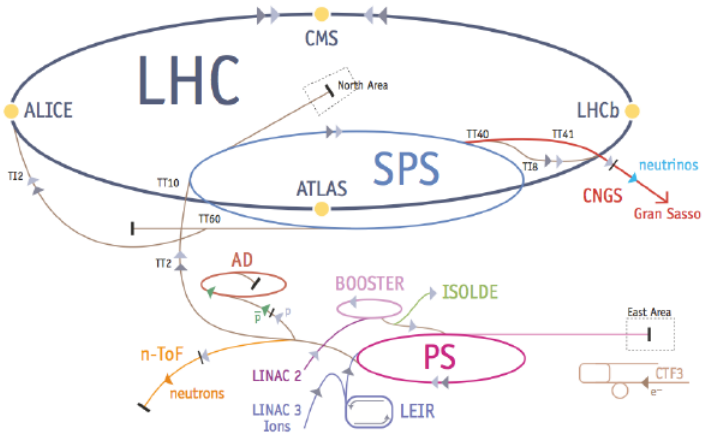

Figure 10: Schematic view of LHC, showing the four interaction points

The process of ion acceleration differs mainly in the initial steps. In particular, lead ions are extracted from a piece of isotopically enriched lead (^{208}Pb) heated up to 500 °C using an electric field. Then, they are accelerated in a linear machine in which the ionization procedure is completed. Ions are then accumulated in a dedicated ion ring (LEIR) and then injected in the Proton Synchrotron.

The tunnel geometry was originally designed for electron-positron beams, with eight crossing points flanked by long straight sections to compensate the high synchrotron radiation losses; even if a proton-proton machine does not have the same radiation loss problem, the already built tunnel has been maintained to limit the costs. However only four of the interaction points have been used, in order to limit disruption of the beams. The main four experiments hosted in these interaction points are:

- *CMS* and *ATLAS* are general purpose experiments mainly designed to test the predictions of the Standard Model (SM) and to look for hints of physics beyond the SM. In particular, one of the main goals was to prove the existence of the Higgs boson.
- *LHCb* is mainly focused on the study of CP asymmetries in processes that involve b-quarks production
- ALICE is the only LHC experiment mainly dedicated to the study of the heavy ions physics .

A schematic view of LHC, showing the four interaction points can be seen in Fig. 10.

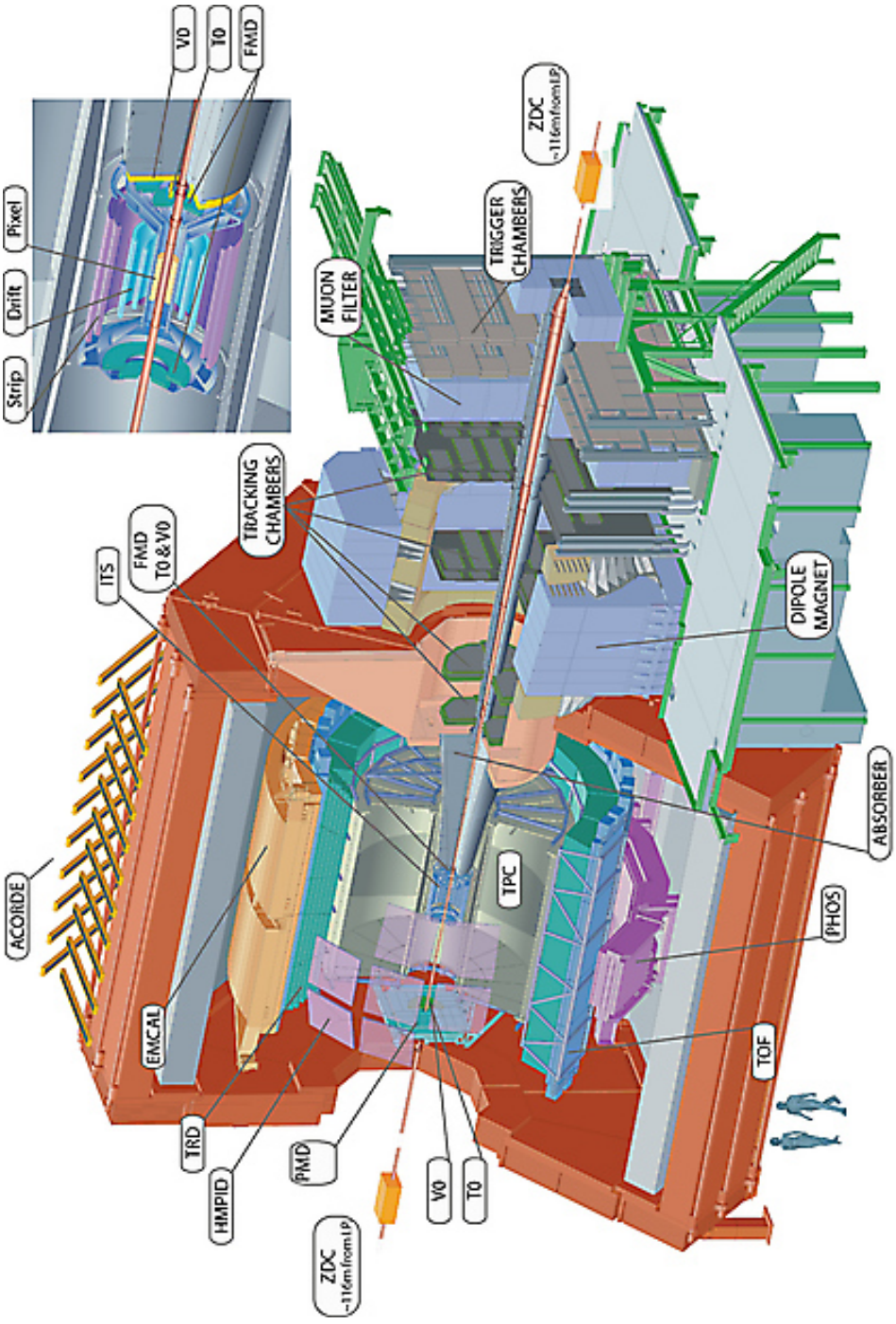

Figure 11: Layout of the ALICE experiment.

2.2 THE ALICE EXPERIMENT

The ALICE experiment is a general purpose heavy-ion experiment mainly focused on the study of strongly interacting matter formed in nucleus-nucleus collisions [34]. ALICE is designed in order to be able to investigate the majority of the experimental observables relevant for the QGP characterization.

The ALICE detector can track particles down to very low momenta (from about 100 MeV/c up to 100 GeV/c) in an environment characterized by a large charged track multiplicity. In addition, a key feature of ALICE is the possibility to identify particles in a wide momentum range using information from different particle identification detectors.

The ALICE layout is shown in Fig. 11. It consists of a central barrel covering the full azimuthal angle in the mid-rapidity region and several systems located at forward and backward rapidity.

The central detectors are located inside a solenoidal magnet generating a magnetic field $B = 0.5\,T$. The central barrel includes the *Inner Tracking System (ITS)* with six layers of silicon detectors, the *Time Projection Chamber (TPC)* which is the main tracking detector, the *Transition Radiation Detector (TRD)* for electron identification and the *Time of Flight detector (TOF)* for the identification of particles at $p_T < 2.5 GeV/c$. Two other detectors with smaller acceptance (both in η and ϕ) complement the central barrel: the *High-Momentum Particle Identification Detector (HMPID)* consisting of an array of ring-imaging Cerenkov counters and the *Photon Spectrometer (PHOS)* which is an electromagnetic calorimeter. The latest designed detector is the *Electromagnetic Calorimeter (EMCal)*. It is placed in the central barrel and it is dedicated to the physics of high-pt photon jets.

The forward detectors (visible on the right part of the Fig. 11) are placed out of the central barrel. The Muon Spectrometer is a detector located at $-4 < \eta < -2.5$ made of an absorber, followed by a spectrometer with a dipole magnet, five tracking stations, an iron absorber and trigger chambers. Additional forward detectors are the *Forward Multiplicity Detector (FMD)* made of silicon strips, the *Photon Multiplicity Detector (PMD)* made of layers of lead converter and the *Zero Degree Calorimeter (ZDC)* consisting of two sets (one at forward and one at backward rapidity) of two hadronic calorimeters (one for protons and one for neutrons) plus one electromagnetic calorimeter: these detectors provide information on the centrality of the collisions.

Two trigger detectors are located on each side of the interaction point: the *V0*, made of two arrays of segmented scintillator counters, and the *T0*, consisting of two arrays of Cerenkov counters.

In the following paragraphs, a more accurated description of the ALICE subdetectors will be provided. For more details on the ALICE apparatus see [34].

2.3 CENTRAL BARREL DETECTORS

2.3.1 Inner Tracking System (ITS)

The Inner Tracking System composition, its limitations in the current version and the strategy for its upgrade will be discussed in Cap. 3.

2.3.2 Time Projection Chamber

The TPC (see left panel of Fig. 12) is the main ALICE tracking detector: it provides charged-particle track reconstruction, particle identification via dE/dx measurement, momentum measurement and, together with the ITS, primary and secondary vertex determination.

It consists of a large cylindrical field cage with an inner radius of about 85 cm and an outer radius of 250 cm, with a length along the beam direction of 500 cm. The drift region is filled with $90 m^3$ of a gas mixture of $Ne/CO_2/N_2$, in which the primary electrons are transported on either side of the central electrode to the end plates.

Typical drift velocities of electrons are about $2.7\,cm\,\mu s^{-1}$ which leads to maximum drift time of about 90 μs.

The electrical field inside the TPC is constant and parallel to the beam direction. A particle traversing the gas creates electrons by ionization. These electrons drift in the electrical field direction to the readout chambers.

Multi-wire proportional chambers with cathode pad readout are mounted into 18 trapezoidal sectors at each end plate.

The TPC allows the study of hadronic and leptonic observables with transverse momenta up to $\sim 100 GeV/c$ in the pseudo-rapidity range $\eta < 0.9$. To measure higher momenta it is necessary to use the TPC in combination with the other tracking detectors (ITS and TRD).

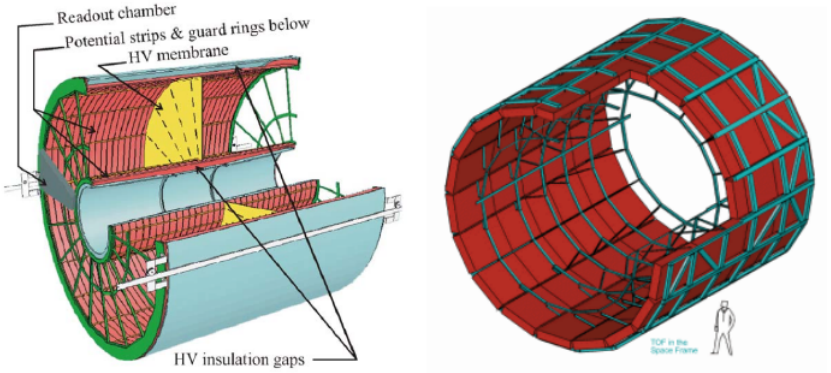

Figure 12: A view of the ALICE Time-Projection Chamber (left) and Time-Of-Flight (right) detector.

2.3.3 Transition-Radiation Detector (TRD)

Transition radiation is emitted when charged particles cross the interface between two media with different dielectric constants.

The TRD is composed of 540 modules: each consisting of a radiator of thickness $\approx 4.8\,\mathrm{cm}$ where x-rays are emitted by charged particles, and a multi-wire proportional readout chamber which detects the x-rays of the transition radiation.

It identifies electrons with momentum above 1 GeV/c in the central barrel, where the pion rejection capability of the TPC is no longer sufficient. This information, in addition to that provided by ITS and TPC, allows the measurements production rates of quarkonia near mid-rapidity, via their e^+e^- decay, as well as the dilepton continuum in PbPb and in pp data. With the impact parameter determination provided by the ITS, it is also possible to measure open charm and beauty from semi-leptonic decays.

With its six layers, the TRD contribute to the global tracking through the central barrel improving the p_T resolution at high momentum.

2.3.4 Time of Flight detector (TOF)

The TOF detector of ALICE covers the central pseudo-rapidity region ($|\eta| < 0.9$) and plays an important role in the identification of pions, kaons and protons in the intermediate momentum range (from 0.2 to 2.5 GeV/c).

The TOF consists of a large area array of Multi-gap Resistive-Plate Chambers (MRPC), a gas detector which is able to guarantee an intrinsic time resolution lower than 60 ps and to cover large areas.

It is positioned on a cylindrical surface (see right panel of Fig. 12) that covers the central barrel over an area of $140\,\mathrm{m}^2$ with 160.000 individual cells at a radius of about 4 m.

The TOF measures the time of flight of the particles which is defined as the time interval between the production of a particle, given by the trigger, and its detection in the MRPC. Particles with different masses can be identified once their times of flight and momenta are know.

The total time resolution of the TOF also includes other contributions coming from the front-end electronics and from the start time. In pp collisions, the total resolution is about 85 ps while in Pb-Pb collisions is significantly larger ($\approx 160\,\mathrm{ps}$) due to the larger uncertainty on the start time.

2.3.5 Other detectors of the central barrel

THE HIGH-MOMENTUM PARTICLE IDENTIFICATION (HMPID) consists of an array of ring-imaging Cherenkov (RICH) detectors with

$|\eta| < 0.6$ and 57.6° of azimuthal coverage. It is positioned at a distance of about 4.9 m from the beam axis and uses a C_6F_{14} radiator and a MWPC with pad readout for detecting ultraviolet photons.

The detector was optimised to extend the useful momentum range for π/K and K/p discrimination, on track-by-track basis, up to 3GeV/c and 5GeV/c respectively.

PHOTON SPECTROMETER (PHOS) is a high resolution electromagnetic calorimeter dedicated to the detection of photons coming from the interaction point and neutral mesons like π_0 and η through their decay in two photons.

It is made of lead crystals, PWO, grouped in five modules and located at 4.6 m from the interaction point and covers approximately $|\eta| \leqslant 0.12$, with a total area of about $8m^2$.

ELECTROMAGNETIC CALORIMETER (EMCAL) covers the pseudo-rapidity range $|\eta| \leqslant 0.7$ and contains 12 modules each consisting of sampling calorimeters made of alternating layers of 1.44 mm Pb and 1.76 mm polystyrene, as scintillating material.

The main physics motivation for the EMCal is to improve the ALICE performances for an extensive study of jet quenching. Indeed, it extends the ALICE capabilities for detecting jets, direct photons and electrons from heavy-flavour decays.

2.4 FORWARD DETECTORS

FORWARD MUON SPECTROMETER. This detector is located around the beam pipe and covers the pseudo-rapidity range $-4.0 \leqslant \eta \leqslant -2.5$.

It consists of a composite absorber located at about 1 m from the interaction point to reduce the background due to π and K decays. The absorber is designed to maximize hadron absorption without introducing too much muon multiple scattering. This is achieved with layers of both high and low Z materials.

Muon tracks are reconstructed by tracking chambers consisting of multi-wire proportional chambers with cathode pad readout. They are embedded in a magnetic field generated by a dipole magnet located outside the L3 magnet.

With the forward muon spectrometer it is possible to study resonances like J/Ψ, Ψ ,Υ, Υ' and Υ'' through their decay into $\mu^+\mu^-$ pairs, and to disentangle them from the continuum given by Drell-Yan processes and semi-leptonic decays of D and B mesons.

ZERO-DEGREE CALORIMETER (ZDC) The ZDC consists of two calorimeters, one for neutrons and one for protons. Two ZDCs are symmetrically installed at 116 m from the interaction point. In this detector quartz fibres (active material) are embedded in a dense absorber of Tungsten (passive material). When a particle crosses the passive material creates a shower which produces Cerenkov radiation in the active material.

It measures the energy of the spectator nucleons and thus provides information on the centrality of the collision, because the zero degree energy decreases with increasing centrality. The ZDC is also used for flow analysis, because it can estimate the reaction plane through the directed anisotropy of spectator neutrons.

PHOTON MULTIPLICITY DETECTOR (PMD). The PMD measures the multiplicity and the spatial distribution of photons on an event-by-event basis in the forward region of ALICE.

It consists of two planes of multi-wire proportional counters with a honey-comb structure separated by a thick lead converter between them. The PMD is placed at 360 cm from the interaction point, on the opposite side of the forward muon spectrometer, covering the region $2.3 \leqslant \eta \leqslant 3.7$.

FORWARD MULTIPLICITY DETECTOR (FMD) It is an array of silicon strip detectors covering the large rapidity region ranges $-3.4 \leqslant \eta \leqslant -1.7$ and $1.7 \leqslant \eta \leqslant 5.1$. The system consists of 51200 silicon strips channels distributed over 5 ring counters formed by 20 or 40 azimuthal sectors. Each sector read out is independent and contains 512 or 256 detector strips at constant radius.

With this detector it is possible to extend the η coverage of multiplicity measurements, to study multiplicity fluctuation on an event-by-event basis and to perform flow analysis.

V0 DETECTOR. The V0 detector is a small angle detector consisting of two arrays of scintillator counters, called V0A and V0C, which are installed on either side of the ALICE interaction point. V0A detector is located 340 cm from the vertex on the side opposite to the muon spectrometer whereas V0C is fixed to the front face of the hadronic absorber, 90 cm from the vertex.

It is used to provide minimum-bias trigger for the central barrel detectors and to estimate the collision centrality via a Glauber fit to the distribution of the summed amplitudes in the V0 scintillator tiles recorded in the event.

T0 DETECTOR. Other two Cherenkov counters, the T0 detectors, are installed to measure the interaction time of the collisions. They are used to generate a start time (T0) for the TOF detector, to

measure the vertex position (with a precision $\pm 1.5\,\mathrm{cm}$) for each interaction and to provide a L0 trigger when the position is within the preset values. The detector consists of two arrays of Cherenkov counters placed at $-72.7\,\mathrm{cm}$ and $375\,\mathrm{cm}$ from the nominal interaction point.

2.5 TRIGGER AND DATA ACQUISITION SYSTEM

2.5.1 Trigger System

The trigger system used by ALICE has been studied to select events with different features depending on the physical interests and is optimized to work both in nucleus-nucleus and pp collisions.

The trigger signals are handled in ALICE by the Central Trigger Processor (CTP). The CTP receives trigger inputs from the trigger detectors and provides trigger signals to readout detectors in case the trigger conditions are fulfilled.

A dedicated processor combines the signals coming from detectors with fast trigger capability (T0, V0, ZDC, SPD, TOF, TRD, PHOS, EMCal, Muons). It operates at several levels to satisfy the individual timing requirements of the different detectors.

A pre-trigger activates the TRD electronics shortly after each interaction ($< 900\,\mathrm{ns}$) while two further levels (L0 at $1.2\,\mu\mathrm{s}$ and L1 at $6.5\,\mu\mathrm{s}$) reduce the event rate depending on the trigger inputs. A final trigger signal called L2 at about $100\,\mu\mathrm{s}$ is then issued after the end of the drift time in the TPC, the slowest detector in ALICE.

The trigger includes a protection against pile-up and an event priority scheme which optimizes both the acceptance of rare triggers and the overall throughput of accepted events. In addition to the hardware trigger system, ALICE can select or reject events by means of the so called High-Level Trigger (HLT). It consists of up to 1000 multiprocessor computers which perform a detailed on-line analysis on complete events. The HLT is also used to reduce the event size by selecting only a fraction of the data for readout (region of interest) or by compressing the complete event information.

2.5.2 DAQ

When the trigger signal reaches the front end electronic of each detector, the data are sent to a farm of 300 individual computers, the Local Data Concentrators (LDC); this is done through an hardware and protocol interface, the DDL, and each computer has an adapter to interface itself to the DDL. The LDC receives thus event fragments, coming from the various detectors, and assembles them into sub-events.

These sub-events are then sent to one of the 40 Global Data Collector computers (GDC), which can process up to 40 different events in parallel. 20 Global Data Storage Servers (GDS) store the data locally before their migration and archive in the CERN computing center where they become available for the off-line analysis.

2.6 ALICE OFFLINE FRAMEWORK

The framework adopted by the ALICE offline project is Aliroot [35], an object-oriented code based on Root [36], a software specifically designed to cope with huge amounts of data coming from high energy experiments.

Root and Aliroot provide the packages to perform event generation, detector simulation, event reconstruction and data analysis. Aliroot in particular includes the geometry of the detectors and their response to the passage of particles.

In this section a description of the main features of the offline framework is given.

2.6.1 AliRoot framework

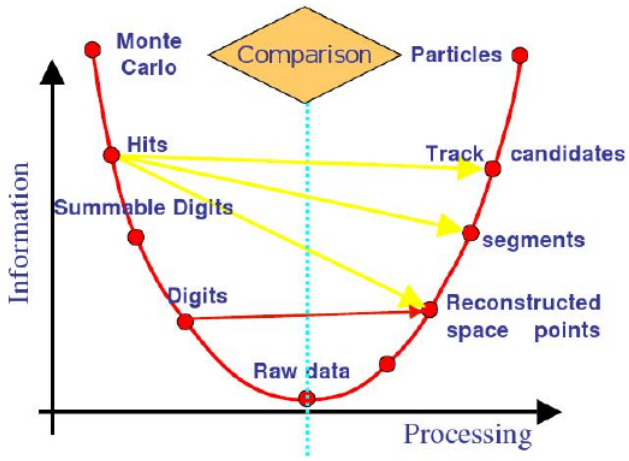

Figure 13: AliRoot data processing framework.

Fig. 13 schematically shows the functionality of the AliRoot framework.

To simulate the particle interaction with the detectors, Aliroot makes use of different Monte Carlo transport programs, like Geant3 [37], Geant4 [38] and Fluka [39].

Simulated events used e.g. for efficiency calculations are generated with Monte Carlo generators. In ALICE, the main generators used for pp collisions are PYTHIA [40] and HERWIG [41] which are

theoretical QCD calculations based on a perturbative approach. The codes adopted for proton-nucleus and nucleus-nucleus collisions are mainly HIJING [42] and DPMJET [43].

The real detector response is then simulated by taking into account the electronic manipulation of the signal, in form of digits, which can then be transformed into the same format provided by the real detectors, i.e. RAW DATA format.

From here on the processing of real and simulated data is indistinguishable, even if simulated data contain of course the full information about the generated particles.

The reconstruction uses digits, i.e. ADC or TDC counts in the form of RAW DATA together with additional information like module number, readout channel number, etc.

A main class provides the user with a simple interface to configure the reconstruction procedure, include or exclude a detector from the run and ensure the correct sequence of the reconstruction steps (local reconstruction for each detector, primary vertex reconstruction, track reconstruction and particle identification, primary and secondary vertex reconstruction from tracks).

The output of the reconstruction is the Event Summary Data (ESD). It contains the reconstructed tracks together with the particle identification information, the reconstructed primary vertex, decays and V0, kink and cascade topologies and particles reconstructed in the calorimeters.

Analysis is the last step performed on data to extract physics results. It starts from the ESD, whose size is about one order of magnitude lower than the corresponding raw data. Analysis performed on the ESD produces Analysis Object Data (AOD), that are used by further analysis steps.

The condition data including parameters such as detector response calibration, bad channel maps, pedestal values and so on, are largely evaluated on line from data collected during normal data taking or during special runs. A part of the condition data, especially for what concerning TPC and TOF, are computed in a dedicated off-line calibration pass.

2.6.2 The GRID

The amount of computing resources necessary to store and process the data generated by the experiment is huge. To cope with this request a distributed computing is necessary. For this reason the Grid computing project was started in 2000.

The Grid [44] is an infrastructure that allows one to distribute computer resources across institutes and universities which take part in the project. The Grid is based on the MONARC model (Models of

Networks Analysis at Regional Centres for the LHC Experiment) and it is organised in different levels or Tiers.

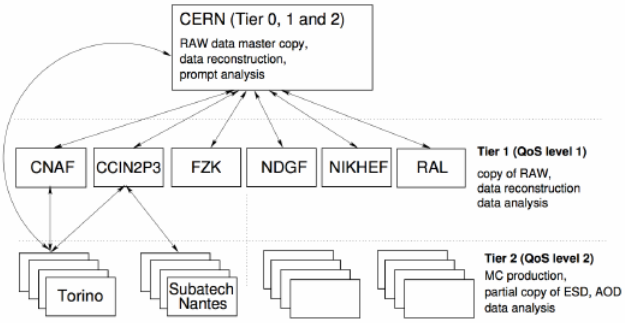

Figure 14: Schematic view of the ALICE computing tasks in the framework of the tiered model.

In this framework, the available computing resources are arranged in different tiers:

- Tier 0 is located at CERN, where the raw data directly coming from the experiments is stored;
- a second copy is distributed among the external Tier 1 centres, which are the biggest computing centres, whose additional task will be also the reconstruction of the events;
- Regional Tier 2 centres contribute to perform Monte Carlo simulations and to produce files ready to be taken by the single users for the analyses.

The interface to the Grid middleware is guaranteed in ALICE by the AliEn environment [44]. The AliEn User Interface (UI), in particular, is used by ALICE users to access the data, send analysis tasks and simulation and monitor their status.

3 THE UPGRADE OF THE INNER TRACKING SYSTEM

Contents

Before the start of the LHC, the nature of the QGP as an almost-perfect liquid emerged from the experimental investigations at CERN SPS and at BNL RHIC. ALICE has confirmed this basic picture, observing the creation of hot hadronic matter at unprecedented values of temperatures, densities and volumes, and exceeding the precision on all significant probes of the QGP that had been measured over the past decade.

Despite this success there are several frontiers, as high precision measurements of rare probes at low transverse momenta, for which the current experimental setup is not yet fully optimized. Detector upgrades combined to a significant increase of luminosity could enormously enhance the physics capabilities.

ALICE is therefore preparing a major upgrade of its apparatus, planned for installation in the second long LHC shutdown (LS2) in the years 2018-2019.

The upgrade strategy is formulated under the assumption that, after LS2, the LHC will progressively increase its luminosity with Pb beams eventually reaching an interaction rate of about 50kHz, i.e. instantaneous luminosities of $\mathcal{L} = 6 \cdot 10^{27} \mathrm{cm}^{-2}\mathrm{s}^{-1}$.

The ALICE long-term physics goals, its experimental strategy and the general upgrade plans are discussed in the ALICE Upgrade Letter of Intent [45].

The main physics topics addressed, which will be briefly discussed in Section 3.2, require the measurement of heavy-flavour hadrons, quarkonia, and low-mass dileptons at low transverse momenta. These

measurements in Pb–Pb collisions are characterized by a very small signal-over-background ratio, which calls for large statistics.

In addition, the large background makes the application of triggering techniques impossible or very inefficient. Besides a very large statistics, these measurements require also a significant improvement of the vertexing and tracking efficiency.

The upgrade plans include:

- A new beampipe with smaller diameter.
- A new, high-resolution, low-material Inner Tracking System (ITS).
- Upgrade of the Time Projection Chamber (TPC), consisting of the replacement of the wire chambers with Gas Electron Multiplier (GEM) detectors and new pipelined read-out electronics.
- Upgrade of the read-out electronics of Transition Radiation Detector (TRD), Time Of Flight detector (TOF) and Muon Spectrometer for high rate operation.
- Upgrade of the forward trigger detectors.
- Upgrade of the online systems, offline reconstruction and analysis framework.
- Introduction of a new detector, the Muon Forward Telescope (MFT), in order to add vertexing capabilities to the current Muon Spectrometer. The MFT consists of five planes of silicon pixel detectors placed in front of the hadronic absorber, covering the acceptance of the Muon Spectrometer. A full description of this new detecor and its specific physics program can be found in the Addendum of the ALICE Letter Of Intent [46].

3.1 CURRENT ITS

The current ITS consists of six layers of silicon detectors placed coaxially around the beam pipe (see Fig. 15) with their radii ranging from 3.9 cm to 43 cm. They cover a pseudorapidity range of $|\eta| < 0.9$ for vertices located within $z = \pm 60\,\text{mm}$ with respect to the nominal interaction point.

To sustain a high particle hit density and to perform an efficient vertex reconstruction, the first two layers were made of Silicon Pixel Detectors (SPD) with state-of-the-art hybrid pixel detectors. The two middle layers are made of Silicon Drift Detectors (SDD) followed by two layers of double sided Silicon Strip Detectors (SSD).

The last four layers have analog readout with PID capabilities through dE/dx measurement in the non-relativistic ($1/\beta^2$) region.

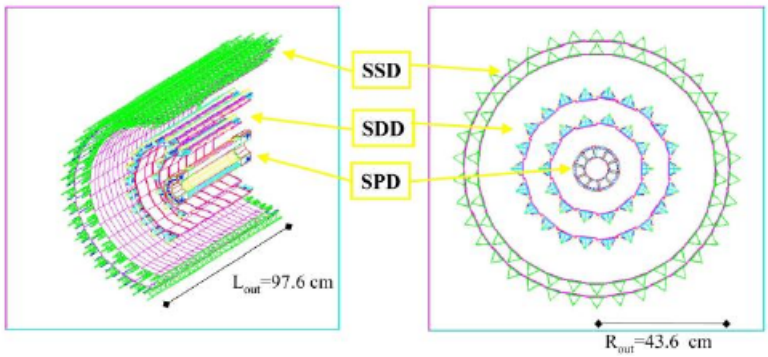

Figure 15: Layout of the Inner Tracking System (ITS) of ALICE. Three Silicon sub-systems are indicated as SPD (pixel), SDD (drift) and SSD (strip).

Parameter	SPD	SDD	SSD
Spatial precision $r\phi$ [μm]	12	38	20
Spatial precision z [μm]	100	28	830
Two tracks resolution $r\phi$ [μm]	100	200	300
Two tracks resolution z [μm]	850	600	2400
Cell size [μm^2]	50×425	150×300	95×40000
Readout channel per module	40960	2×256	2×768
Total number of modules	240	260	1698
Material Budget X/X_0 %	1.14	1.26	0.83
Radius [cm]	3.9 7.6	15.0 23.9	38.0 43.0

Table 1: Main specifications of the present ALICE ITS.

The layer parameters were optimized for efficient tracking performance in combination with the TPC and high precision in determining the charged particle distance of closest approach to the primary vertex.

Thus, the first layer has a radius as small as possible, defined by the radius of the beam pipe. The outermost radius was defined in a way to optimize the track matching efficiency with the TPC. Main layer parameters are shown in Table 1.

Here follows a brief description of the three different types of detector located in the ALICE ITS.

3.1.1 Silicon Pixel Detector

The SPD is based on a two dimensional matrix of reverse biased silicon diodes bump-bonded to readout chips.

The sensor matrix includes 256×160 cells measuring 50 μm ($r\phi$) by 425 μm (z) with a thickness of 200 μm; each readout chip is connected to 256×32 detector cells and has a thickness of 150 μm.

Each pixel cell contains its own amplifier with leakage current compensation followed by a discriminator.

A cooling system based on the evaporation of C_4F_{10} is mounted in contact with the detector in order to allow it to operate at room temperature.

Each of the 1200 front-end chips generates a Fast-OR signal when at least one of its pixel is hit by a particle; this Fast-OR signal contributes to the Minimum Bias (MB) trigger.

3.1.2 Silicon Drift Detector

The Silicon Drift Detectors (SDD) equip the two intermediate layers of the ITS, where the charged particle density is expected to reach up to $7\,cm^{-2}$.

They have a sensitive area of $70.17(r\phi) \times 75.26(z)\,mm^2$ and a total area of $72.50 \times 87.59\,mm^2$. The sensitive area is split into two drift regions by the central cathode strip to which a HV bias of $-2.4\,kV$ is applied.

In each drift region and on both detector surfaces, 291 p^+ cathode strips, with $120\,\mu m$ pitch, fully deplete the detector volume and generate a drift field parallel to the wafer surface.

The operating principle is based on the measurement of the time necessary for the electrons produced by an ionizing crossing particle to drift from the generation point to the collecting anodes.

The impact position of the crossing particle is determined in two dimensions:

- one coordinate is estimated using the electron *drift time* from the point where charge is generated to the anodes;
- the other is provided by the *centroid position* of the charge distribution collected by the anodes.

Moreover the total charge collected from the anodes is proportional to the energy deposited in the detector by the crossing particle and this can be exploited for particle identification via dE/dx in the non-relativistic region.

3.1.3 Silicon Strip Detector

The two outer layers are fundamental for the matching of tracks from the TPC to the ITS; they consist of double-sided Silicon Strip Detectors (SSD) mounted on carbon-fibre support structures.

The basic unit is the module, namely the sensor assembled with its read-out front-end electronics, which consists of two hybrids.

A strip detector is an arrangement of strip-like shaped implants acting as charge collecting electrodes. Placed on a low doped fully

depleted silicon wafer these implants form a one-dimensional array of diodes. By connecting each of the metalized strips to a charge sensitive amplifier a position sensitive detector is built.

Two dimensional position measurements can be achieved by applying an additional strip orientated perpendicularly on the wafer backside resulting in a double sided technology.

3.2 PHYSICS MOTIVATION FOR THE ITS UPGRADE

The long-term physics goal of ALICE is to study and provide a characterisation of the Quark Gluon Plasma (QGP) state of matter. To achieve this goal, high statistics measurements are required, as these will give access to the very rare physics channels needed to understand the dynamics of this condensed phase of QCD.

The ALICE experimental strategy and the upgrade plans are discussed in the ALICE Upgrade Letter of Intent [45], its addendum [46] and in the ALICE Inner Tracking System Upgrade Technical Design Report [47] . The two main open questions concerning heavy-flavour interactions with the QGP medium are:

- Thermalisation and hadronization of heavy quarks in the medium, which can be studied by measuring the heavy-flavour baryon/meson ratio, the strange/non-strange ratio for charm, the azimuthal anisotropy v_2 for charm and beauty mesons and the possible in-medium thermal production of charm quarks.

  In this respect, the new ITS will have a significant impact on the following measurements, permitting for the first time the access to some specific physics channel, such as:

  - D mesons, including D_s
  - Charm and beauty baryons, Λ_c and Λ_b . The former will be measured, for the first time, through the decay $\Lambda_c \to pK^-\pi^+$, the latter will be measured through the decay $\Lambda_b \to \Lambda_c + X$
  - Baryon/meson ratios for charm (Λ_c/D) and for beauty (Λ_b/B)
  - Study of the elliptic flow of charmed and beauty mesons and baryons down to low p_T

- Heavy-quark in-medium energy loss and its mass dependence, which can be addressed by measuring the nuclear modification factors R_{AA} of the p_T distributions of D and B mesons separately in a wide momentum range, as well as heavy flavour production associated with jets.

  The new ITS will significantly improve or make accessible for the first time the following measurements in Pb-Pb collisions

- Measurements of beauty production via the decay channels $B \to D + X$, $D^0 \to K\pi$,
- Measurements of beauty production via displaced $J/\psi \to ee$.
- Improve measurement of single displaced electrons.
- Improve beauty decay vertex reconstruction, using any of the previous three channels plus an additional track.

Moreover, the new ITS will also allow the measurement of low-mass dielectrons. This measurement gives access to:

- Thermal radiation from the QGP, via real and virtual photons detected as dielectrons.
- In-medium modifications of hadronic spectral functions related to chiral symmetry restoration, in particular for the ρ meson in its e^+e^- decay mode.

3.3 CURRENT ITS LIMITATIONS

As far as the physics performance in heavy flavour detection is concerned, the current ITS has significant limitations.

For example, the current ITS has an impact parameter resolution larger than the decay length of Λ_c ($c\tau = 60\mu m$) which is the most abundantly produced charm baryon, making it inaccessible in Pb–Pb collisions. Thus in ALICE the study of charm baryons is not feasible with the current setup. The resolution on the impact parameter of the curent ITS is shown in Fig. 16.

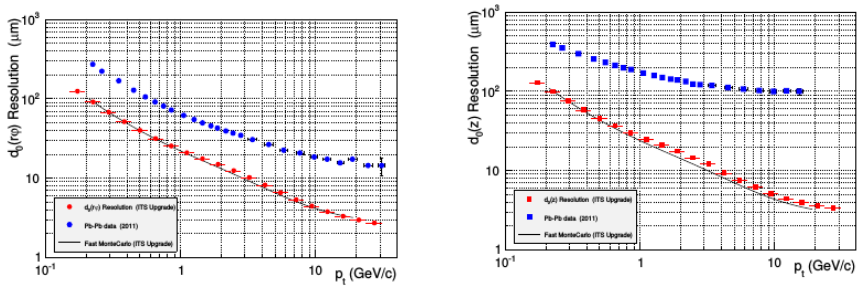

(a) Impact parameter resolution as a function of p_t in the transverse plan

(b) Impact parameter resolution as a function of p_t in z direction

Figure 16: Impact-parameter resolution for primary charged pions as a function of the transverse momentum for the current ITS and the upgraded ITS in the transverse plane (Fig. 16a) and in the longitudinal direction (Fig. 16b). [47]

Another disadvantage of the current ITS is its limited readout capabilities: a maximum rate of 1 kHz (with dead time close to 100%),

Observable	Current, $0.1\,nb^{-1}$		Upgrade, $10\,nb^{-1}$	
	p_T^{min} [Gev/c]	statistical uncertainty	p_T^{min} [Gev/c]	statistical uncertainty
Heavy Flavour				
D Mesons R_{AA}	1	10%	0	0.3%
D_s Mesons R_{AA}	4	15%	< 2	3%
D Meson from B R_{AA}	3	30%	2	1%
J/ψ Meson from B R_{AA}	1.5	15%	1	5%
B^+ yield	not accessible		3	10%
Λ_c R_{AA}	not accessible		2	15%
Λ_c/D^0 ratio	not accessible		2	15%
Λ_b yield	not accessible		7	20%
D Meson v_2 $(v_2 = 0.2)$	1	10%	0	0.2%
D_s Meson v_2 $(v_2 = 0.2)$	not accessible		< 2	8%
D Meson from B v_2 $(v_2 = 0.05)$	not accessible		2	8%
J/ψ Meson from B v_2 $(v_2 = 0.05)$	not accessible		1	60%
Λ_c v_2 $(v_2 = 0.15)$	not accessible		3	20%
Dielectron				
Temperature (intermediate mass)	not accessible			10%
Elliptic flow $(v_2 = 0.1)$	not accessible			10%
Low mass spectral function	not accessible		0.3	20%
Hypernuclei				
${}^3_\Lambda H$ yield	2	18%	2	1.7%

Table 2: Summary of the physics reach foreseen after the ITS upgrade: minimum accessible p_T and relative statistical uncertainty in Pb-Pb collisions for an integrated luminosity of $10\,nb^{-1}$. For heavy flavour, the statistical uncertainties are given at the maximum between $p_T = 2\,GeV/c$ and p_T^{min}. For elliptic flow measurements, the value of v_2 used to calculate the relative statistical uncertainty σ_{v_2}/v_2 is given in parenthesis. The case of the program up to Long Shutdown 2, with a luminosity of $0.1\,nb^{-1}$ collected with minimum-bias trigger, is shown for comparison.

irrespective of the detector occupancy. This is a crucial limitation since it prevents ALICE to exploit the full Pb-Pb collision rate of 8 kHz, which the LHC can deliver presently. This results in inadequate statistics, specially for the physics channels which cannot be selected by a trigger.

Finally, the present ITS is inaccessible for maintenance and repair inteventions during the yearly LHC shutdowns. This could lead to a significant compromise in maintaining high data quality. So, it is a high priority in the design of the upgraded ITS to have rapid accessibility.

The physics goal after the upgrade for various observables is summarised in Tab. 2 in terms of minimum accessible p_T and of statistical uncertainties, for comparision the case of the programme up to Long Shutdown 2 is also shown.

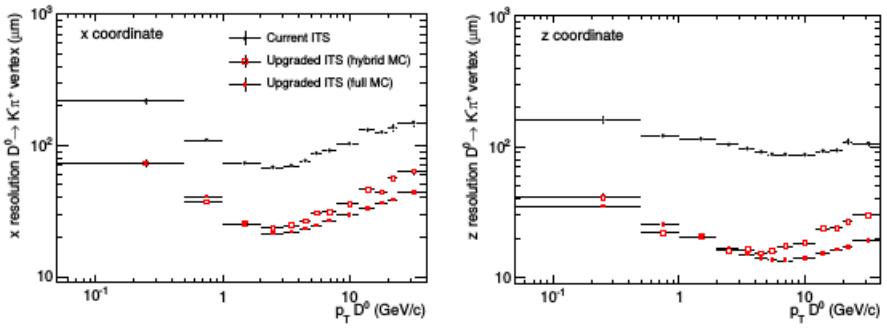

Figure 17: $D^0 \to K^-\pi^+$ secondary vertex position resolutions for current and upgrade scenarios: x (left) and z (right) coordinates. [47]

3.3.1 Example: Resolution on secondary vertex for D^0 meson and prompt charm R_{AA}

In this section an example of performance studies for heavy flavour detection with the upgraded ITS is presented. In particular the case of the D^0 meson is taken into account showing the improvements achievable after the upgrade in the resolution on the secondary vertex.

The resolutions on the reconstructed position of the $D^0 \to K^-\pi^+$ decay vertex are shown in Fig. 17 for the current ITS, the upgraded ITS with full simulation of the new detector and with the *Hybrid method* (i.e. appling the detector performance of the upgraded ITS to full simulations of the current ITS). With the upgraded ITS, the resolution improves by a factor of about three for x (and y) coordinates and about six for z.

Fig. 19a shows the measurement of D meson R_{AA} in central collision using ALICE data from 2010 and 2011. The analysis was restricted to $p_T > 2GeV/c$ with the 2010 data and to $p_T > 1GeV/c$ using higher-statistics data from the 2011 Pb–Pb run [48]. Reaching zero transverse momentum seems to be precluded with the current setup, due to the large background level. As shown in Fig 18 , the upgrade of the ITS will enlarge significantly the background to noise ratio in the πk mass invariant spectrum increasing the signal to noise ratio and allowing to exploit regions of p_T not accessible with the current setup.

In addition, the present accuracy of the R_{AA} measurement is limited to 40% by the systematic uncertainties on the B feed-down correction, the signal yield extraction, and the tracking efficiency.

All these contributions could be substantially reduced with an upgraded vertex detector. Fig. 19b shows the nuclear modification factor of prompt D^0 with the systematic and the statistical uncertainties expected for 8.5×10^9 central $(0-10\%)$ Pb-Pb events, corresponding to $\mathcal{L}_{int} = 10nb^{-1}$.

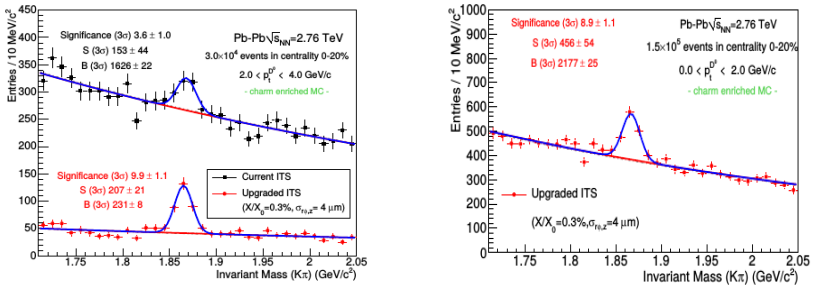

(a) (b)

Figure 18: $D^0 \to K^-\pi^+$. Fig 18a: comparison between the invariant mass distributions of D^0 candidates with $2 < p_t < 4 GeV/c$ obtained from the analysis of $\sim 3 \times 10^4$ central $(0-20\%)$ Pb-Pb events at $\sqrt{s_{NN}} = 2.76 TeV$ (HIJING events enriched with charm signals) with the current and upgrade scenarios. Fig 18b: invariant mass distribution in $0 < p_t < 2 GeV/c$ obtained from the analysis of $\sim 1.5 \times 10^5$ central (0–20%) Pb–Pb events at $\sqrt{s_{NN}} = 2.76 TeV$ (same as above) with the upgrade scenario. [49]

The study of beauty mesons and beauty baryons would also be possible with the upgraded ITS, since their production would be enhanced in the upgrade scenario, thanks to the high interaction rate and the improved impact parameter resolution.

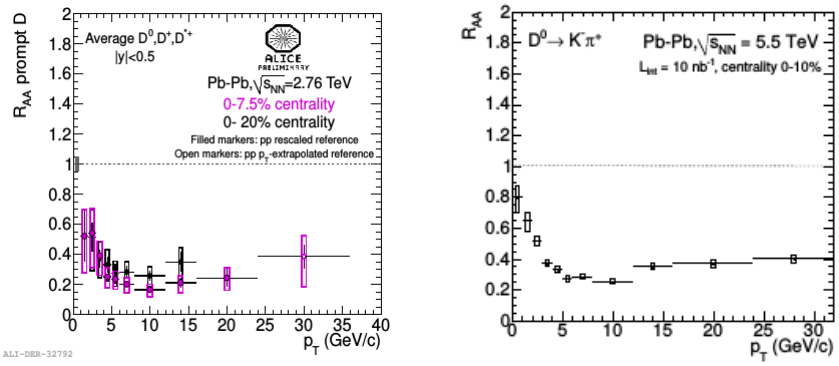

(a) Average D meson R_{AA} vs p_T calculated with ALICE 2010 and 2011 data

(b) Prompt D^0 meson R_{AA} vs p_T with $\mathcal{L}_{int} = 10 nb^{-1}$

Figure 19: In Fig. 19a a comparison of average D meson R_{AA} vs p_T in $|y| < 0.5$ in $0-20\%$ (2010 data) and $0-7.5\%$ (2011 data) central Pb–Pb events [48]. In Fig. 19b the nuclear modification factor of prompt D^0 mesons in central Pb-Pb for $\mathcal{L}_{int} = 10 nb^{-1}$ with statistical and systematic uncertainties.

3.4 ITS UPGRADE OVERVIEW

Based on the upgrade physics motivations and the limitations of the present ITS, the design motivations for the upgraded ITS are:

- Highly efficient tracking, both in standalone mode and in association with the TPC, over an extended momentum range, with special emphasis on very low momenta.
- Very precise reconstruction of secondary vertices from decaying charm and beauty hadrons.

The requirement for an efficient tracking in ITS standalone mode and in combination with the TPC drove the design and geometry of the layers of the upgraded ITS. This translates to a barrel geometry with seven layers and their radii optimized to fit the tracking requirements.

As demonstrated in the ALICE ITS Upgrade CDR [49], the two possible options for the ITS Upgrade were as follows:

- inner layers consisting of silicon pixel detectors with binary readout and the outer layers equpped with silicon strip detectors with analog readout measuring the ionization in silicon
- all layers consisting of monolithic pixel detectors.

Recent studies [47] on the assessment of PID capabilities motivated the selection of the layout consisting of all layers of monolithic pixel detectors with binary read-out (see sec. 3.4.1).

3.4.1 Upgrade concept

In this section, the key features of the ITS upgrade will be discussed and compared to the present ITS.

SMALLER BEAM PIPE The vacuum beam pipe represents the main interface between the experiment and the LHC. The present beam pipe is 4.82 m long with a central section made of a straight beryllium tube of length 3.95 m, wall thickness 0.8 mm and outer radius 29.8 mm [50].

Current studies indicate that it should be possible to reach a beampipe inner radius of 17.2 mm for the upgrade scenario, compared to the present value of 29 mm.

Since its feasibility is yet to be confirmed by further studies, a conservative number of 19 mm is assumed for the beampipe inner radius. Thus, the baseline scenario for the ALICE upgrade includes the installation of a new beam pipe with a wall thickness of 0.8 mm and an outer radius of 19.8 mm.

MATERIAL BUDGET REDUCTION will allow the tracking performance and momentum resolution to be significantly improved.

The use of Monolithic Active Pixel Sensors (MAPS) (see chap. 4) will allow the silicon material budget per layer to be reduced by a factor of seven in comparison to the present ITS (50 μm instead of 350 μm).

The lower power consumption and a highly optimised scheme for the distribution of the electrical power and signals will allow the material budget of the electrical power and signal cables to be reduced by a factor of five.

Combining all the elements together, it should be possible to build a detector with a radiation length of $0.3\%\,X_0$ per layer or better for the three Inner Layers.

Achieving such a low material budget is particularly critical for the first detection layer, since it affects strongly the impact parameter resolution at low p_T where the resolution is mainly determined by multiple Coulomb scattering.

NO MEASUREMENTS OF ENERGY LOSS. In order to asses the benefit of ITS PID capabilities studies have been carried out on benchmark measurements of the ALICE upgrade programme that should be most sensitive to low-momentum PID, namely the low-mass di-electron analysis and the $\Lambda_c \rightarrow p\,K\,\pi$ reconstruction.

These studies confirmed that the new ITS with the same PID capabilities as the current ITS would have only a marginal improvement on the selected benchmark channels.

	Inner Barrel			Outer Barrel			
	Inner Layers			Middle Layers		Outer Layers	
	L. 0	L. 1	L. 2	L. 3	L. 4	L. 5	L. 6
Radial position (min.) [mm]	22.4	30.1	37.8	194.4	243.9	342.3	391.8
Radial position (max.) [mm]	26.7	34.6	42.1	197.7	247.0	345.4	394.9
Length (sensitive area) [mm]	271	271	271	843	843	1475	1475
Pseudo-rapidity coverage	$\pm$ 2.5	$\pm$ 2.3	$\pm$ 2.0	$\pm$ 1.5	$\pm$ 1.4	$\pm$ 1.4	$\pm$ 1.3
Active area $[cm^2]$	421	562	702	10483	13104	32105	36691
Nr. Pixel Chips	108	144	180	2688	3360	8232	9408
Material Budget $X/X_0\%$	0.3	0.3	0.3	0.3	0.3	0.3	0.3
Intrinsic Resolution $(r\phi, z)$ $[\mu m]$	(5,5)	(5,5)	(5,5)	(5,5)	(5,5)	(5,5)	(5,5)

Table 3: Specifications of the Upgraded ITS

LOWER READ-OUT TIME. The present ITS features a maximum read-out rate of 1 kHz. The new detector is designed to be able to read the data related to each individual interaction up to a rate of 100 kHz for Pb-Pb collisions and 400 kHz for pp collisions.

Monolithic Active Pixel Sensors (MAPS) implemented using the 0.18 μm CMOS technology of TowerJazz have been selected as the technology for all layers.

The basic MAPS element is the Pixel Chip consisting of a single silicon die of about 15 $mm \times 30$ mm, which incorporates a high-resistivity silicon epitaxial layer (sensor active volume), a matrix of charge collection diodes (pixels) with a pitch of the order of 30μm, and the electronics that perform signal amplification, digitisation and zero-suppression.

3.4.2 Layout overview

The Upgraded ITS will have a barrel geometry with seven layers consisting of monolithic pixels. The main characteristics in terms of geometrical parameters, material budget and detector intrinsic resolution are quoted in Table 3. Parameters referring to the present ITS are presented in table 1.

The layers in the upgraded ITS are grouped into two separate barrels: the Inner Barrel (IB), containing the three innermost layers and the Outer Barrel (OB), with the four outermost layers.

Fig. 20a shows the layout (top panel) and the schematic view of the cross section (bottom panel) of the Upgraded ITS.

Each layer is segmented azimuthally in mechanically independent units called *Staves*.

The Staves are fixed to a support structure to form Half-Layers. A Stave represent a complete detector element and consists of:

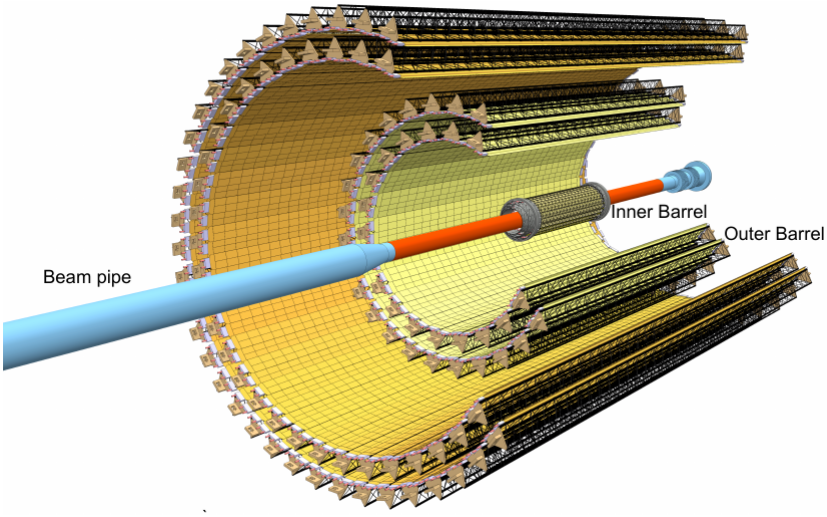

(a) Layout of the upgraded ITS

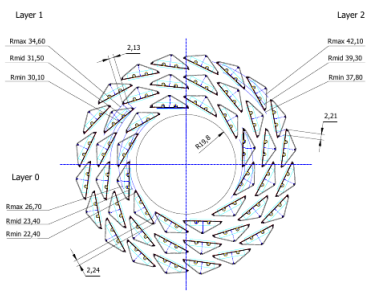

(b) Inner Barrel.

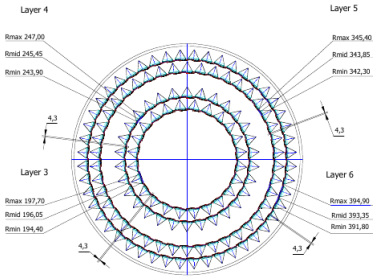

(c) Outer Barrel.

Figure 20: In the top panel (Fig. 20a) the layout of the new ITS is shown. In the two bottom panels a schematic view of the cross section of the Inner Barrel (Fig. 20b) and of the Outer Barrel (Fig. 20c) are presented.

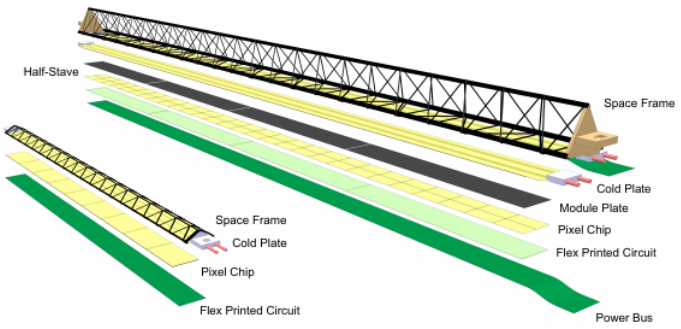

Figure 21: Schematic drawing of the Inner Barrel (left) and Outer Barrel (right) Staves.

- *Space Frame*: a carbon fiber support structure for a single stave.
- *Cold Plate*: carbon ply to embed the cooling pipes.
- *Hybrid Integrated Circuit*: hosts the Flexible Printed Circuit (FPC) on which the pixel chips are bonded.
- *Half-Stave*: the Outer Barrel Stave is further segmented in azimuth in two halves called Half-Stave. Each Half-Stave consists of a number of modules glued on a common cooling unit.
- *Module*: the Outer Barrel staves are also segmented longitudinally to Modules. Each Module consists of a Hybrid Integrated Circuit glued onto a carbon plate named as Module Plate.

The Staves for the Inner Barrel and the Outer Barrel are illustrated schematically in Fig. 21

4 MONOLITHIC ACTIVE PIXEL SENSORS

Contents

Particle sensors and their associated readout electronics, used for vertexing and tracking detection systems in particle physics experiments, have very demanding requirements in terms of granularity, material thickness, read-out speed, power consumption and radiation hardness .

The development of sensors based on silicon (Si) semiconductor technology and of readout electronics based on CMOS technology (application-specific integrated circuits, ASICs) in the 1980s revolutionised the implementation of such detection systems. This technology can be used to match the majority of the above requirements.

Nowadays Si microstrip and pixel sensors are at the heart of the vast majority of particle tracking systems used in particle physics experiments. Nevertheless, compromises exist in the implementation of this technology. Perhaps the most significant is the interface between the sensor and the readout electronics, i.e. they are typically separate components. For example, the present Si pixel detectors used in the innermost layers of the LHC experiments (ATLAS, CMS, LHCb and ALICE) all consist of Si pixel sensors bump-bonded to CMOS read-out electronics.

This technology can be optimised by thinning both sensor and readout chip, as well as by reducing the bump-bonding pitch as much as possible. Nevertheless there are technical limitations and these are

being reached with the present detectors. To go beyond these limitations and build detection systems with, for example, higher granularity and less material thickness, requires the development of a new technology.

One way to achieve this goal is to merge both sensor and read-out electronics into a single detection device. This is the approach taken with CMOS Monolithic Active Pixels Sensors (MAPS).

4.1 INTERACTION OF PARTICLES WITH SILICON SENSORS

The detection principle of semiconductor detectors is based on the detection of charge carriers generated by the interaction of radiation or charge particles with the material (sensor) of the detector. The interaction process depends on the type, charge or energy of the particles traversing the sensor material.

4.1.1 Interaction with charged particles

The charged particles traversing the sensor undergo scattering processes with the electrons of the interacting medium. These processes are dominant for particles heavier than electrons and can be characterized by the average energy loss suffered by the particle, expressed by the Bethe-Bloch formula [51].

$$-\frac{dE}{dx} = kz^2 \frac{Z}{A\beta^2}\left[\frac{1}{2}\ln\frac{2m_e c^2\beta^2\gamma^2 T_{max}}{I^2} - \beta^2\right] \tag{12}$$

with

$$k = 4\pi N r_e^2 m_e c^2$$

where:

- N is the Avogadro number
- z is charge of the traversing particle in units of the electron charge
- r_e is the classical electron radius
- $m_e c^2$ is the electron rest mass energy
- Z is the atomic number of the sensor material
- A is the atomic mass of the sensor material
- I is the mean excitation energy

- β is the velocity of the crossing particle in unity of speed of light
- γ is the Lorentz factor $\sqrt{\frac{1}{1-\beta^2}}$

and T_{max} is the maximum kinetic energy which can be transferred to an electron by a particle of mass M, given by:

$$T_{max} = \frac{2m_e c^2 \beta^2 \gamma^2}{1 + 2\gamma m_e/M + (m_e/M)^2} \tag{13}$$

For particles much heavier than electrons, $M \gg m_e$, the energy loss mainly depends on β and γ. However, at high energy, the Lorentz factor (γ) can have comparable magnitude to the ratio m_e/M and cannot be neglected.

For electrons and positrons, corrections to the Bethe-Bloch formula are required since they interact in the traversing medium with identical particles (i.e. electrons) and additional energy loss mechanisms, like bremsstrahlung, have to be considered.

For low energies, the energy loss is dominated by the factor $1/\beta^2$. For a particle having $\beta\gamma \sim 3$, the energy loss from the Bethe-Bloch equation (12) reaches a minimum. A particle in such energy conditions is called a *minimum ionizing particle (MIP)*.

The number of charge carriers (electrons and holes) generated in the semiconductor by the traversing particle is determined by dividing the deposited energy by the mean energy required for ionization (3.6 eV for silicon).

The ionization process during the passage of a charged particle through matter is subject to statistical fluctuation resulting in fluctuations of the energy loss in the medium. The equation (12) gives the average energy loss per path unit. The probability distribution of the energy loss depends on the thickness of the absorber. For thick absorbers, the energy loss distribution has a Gaussian shape. In thin absorbers, the fluctuation is higher and the distribution is asymmetric. For silicon sensors, the energy loss distribution was calculated by Landau [52] and Vavilov [53].

Apart from energy loss, charged particles traversing a detector suffers from *Multiple Coulomb Scattering*. This results in small deviations of the track due to successive small angle deflections symmetrically distributed around the incident direction. The scattering angle follows roughly a Gaussian distribution [54] with a root mean square of

$$\sqrt{\langle\theta^2\rangle} = \frac{13.6\,MeV}{\beta\, p\, c}\, z \sqrt{\frac{X}{X_0}} \left[1 + 0.038 \log \frac{X}{X_0}\right] \tag{14}$$

where β, p and z are the velocity, momentum and charge of the particle, respectively and the ratio X/X_0 gives the thickness of the absorption medium in units of radiation length.

4.1.2 Interaction with electromagnetic radiation

The behaviour of photons is dramatically different from that of charged particles, in particular their lack of electric charge makes impossible inelastic collisions with atomic electrons. Electromagnetic radiation interacts in semiconductor detectors in the form of three main processes:

- Photoelectric effect
- Compton effect
- Pair production

In these interactions, the incident radiation is either completely absorbed in the sensor material, like in photoelectric effect and pair production, or is scattered (Compton effect).

The photons which pass straight through are, therefore, those which have not suffered any interactions at all. The result is that a monochromatic photon beam traversing the sensor material does not change its energy but it is attenuated in intensity:

$$I(x) = I_0 e^{-x/\mu} \tag{15}$$

where I_0 is the incident beam intensity, x is the thickness of the traversed material and μ is attenuation length (characteristic of the medium and depending on the photon energy).

At low energies (below 100 keV for silicon), photoelectric effect is the dominant process. At higher energies, the scattering process becomes dominant. Silicon is used for photon detection up to energies of about 100 keV. A detailed description of these processes can be found in literature [55].

4.2 DETECTION PRINCIPLE

The simplest semiconductor detector is based on a reverse biased junction. Electromagnetic radiation interacting with the semiconductor would produce electron-hole pairs near the point of interaction whereas charged particles would produce electron-hole pairs along their path through the semiconductor. The produced charge carriers move by drift due to the applied reverse bias or by diffusion due to concentration variation and are collected by the electrodes associated to the front end readout electronics.

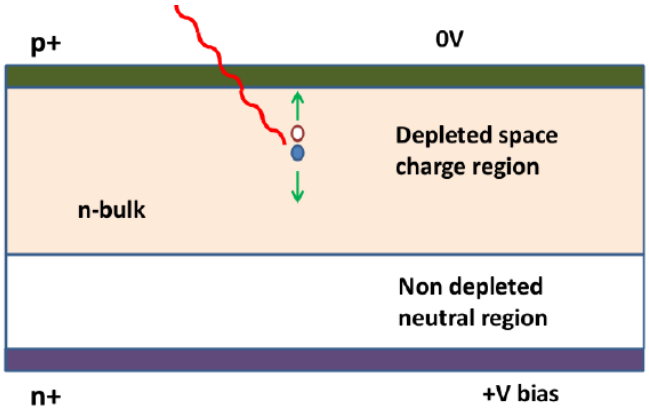

Figure 22: Schematic structure of a reversely biased semiconductor diode used as photon detector

4.3 MONOLITHIC ACTIVE PIXEL SENSOR

As we have already mentioned in chapter 3 all the innermost vertexing and tracking detectors in the experiments at the LHC (ATLAS, CMS, LHCb, ALICE) use state of the art hybrid pixel detectors. A hybrid pixel detector is schematically illustrated in left panel of Fig. 23. In these detectors, the silicon sensor and the front end readout electronics are separate components attached by bump-bonding.

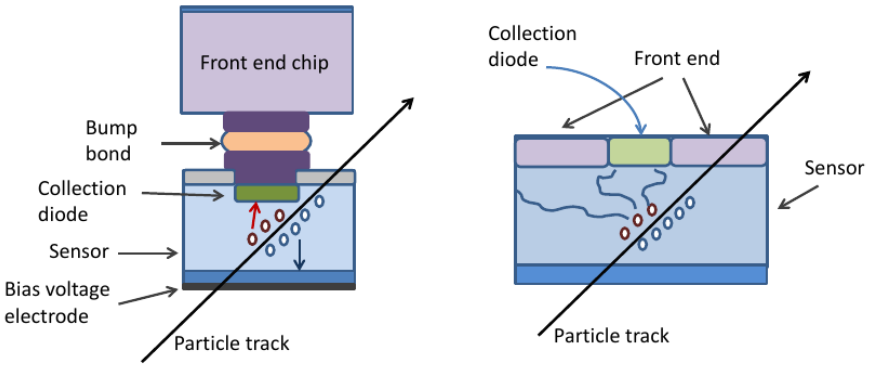

Figure 23: (Left): Hybrid pixel. The sensor and the front end chip are two separate components attached by a bump bond. (Right): Monolithic pixel. The sensor and the frontend are developed on the same silicon substrate

The advantage of this technology is that the sensor and the frontend chip can be optimized separately and sensor materials other than silicon can be used. The technology for the different parts of the detector are provided by standard industrial processes and are available from a large number of industrial vendors. However, there are technical limitations of this technology and the hybrid pixel detectors

used in the LHC experiments are already optimized close to these limits.

Further improvement can be done in terms of higher granularity and reduced material budget if, for example, the sensor and the front end readout are implemented on a single silicon substrate. This approach led to the development of CMOS Monolithic Active Pixel Sensors (MAPS). A schematic design of MAPS is shown in right panel of Fig.23, to compare this basic difference with the hybrid pixels.

Extensive research and development in the last decade on MAPS made it an option for future vertexing and tracking silicon detectors. There are limitations of MAPS with respect to radiation hardness and readout speed due to which they are still not suitable for the LHC experiments like ATLAS, CMS and LHCb. But they can be a very good option in ultra-relativistic heavy ion experiments like ALICE where the radiation tolerance and readout requirements are less stringent. The ULTIMATE sensor [56] developed for the STAR Heavy Flavor Tracker (HFT) at RHIC was the first application of MAPS in a heavy-ion experiment. However, this sensor developed with AMS 0.35 μm technology does not satisfy the requirements of ALICE ITS upgrade, especially in terms of radiation hardness and readout time.

These limitations could be overcome by the 0.18 μm technology provided by TowerJazz which is the technology selected for the ALICE ITS upgrade.

4.4 DETECTION PRINCIPLE IN MAPS

The detection principle in standard MAPS is based on charge collection by diffusion. The different doping concentrations in different layers of MAPS facilitates the diffusion process. The charge carriers (electron-hole pairs) are generated in the epitaxial layer by the impinging particles. The electrons generated are deflected by the substrate due to a potential barrier formed between the lightly doped p-type epitaxial layer and the heavily doped p-type substrate. Similarly, a potential barrier exists between the lightly doped epitaxial layer and the heavily doped p-wells of the NMOS transistors.

This results in the containment of the majority of the electrons within the epitaxial layer which diffuse randomly. Diffusing electrons are then collected as a signal when they reach the built-in electric field at the junction formed by the n-well of the sensing diode and the p-type epitaxial layer.

In standard implementations, the sensing diode is an n-well normally used as the substrate of PMOS transistors. As a consequence, only NMOS transistors can be used in the pixel area. In fact, any PMOS transistor requires an additional n-well that competes with the sensing diode in collecting the signal charge. The front-end elec-

tronics located in the pixel must fully rely on NMOS devices, so only simple, low-gain amplifiers or source followers can be implemented. Hit discrimination, which requires more sophisticated signal processing, cannot be performed at the pixel level and the full matrix must be scanned during the read-out phase.

4.4.1 Front end readout

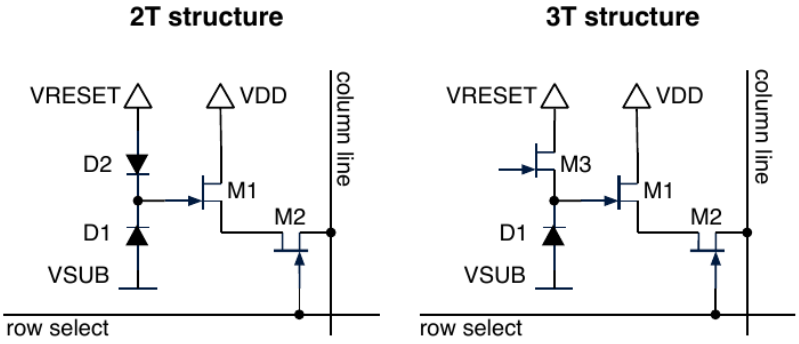

Figure 24: : Simplified schematic drawing of the 2T and 3T pixel structures, as used in the rolling-shutter read-out scheme.

The most common in-pixel architectures are the so called 2T and 3T architectures, as shown in Fig. 24. The architecture consists of a source follower transistor (M1) connected to the sensing diode. The charge collected by the sensing diode results in a voltage drop at the gate of the source follower transistor which acts as a voltage buffer.

The output of the buffer is connected to a second transistor (M2) which acts as a switch. This switch enables the read out of the buffer output at the end of column circutry.

The sensing diode suffers a continuos voltage decay due to leakage current since the parasitic capacitance of the collection diode discharges continuously. This is compensated at regular intervals by connecting the diode to a reference potential using a reset transistor (M3), in case of a 3T structure. The reset transistor is replaced by a forward biased diode in a 2T structure (self-bias).

Such an arrangement is often readout by a method called the *rolling shutter readout*: rows are read out one after the other by selecting the row switches (M2) and, in case of 3T, applying the reset pulse shortly after.

In this way each row integrates the signal between two consecutive passings of the row select signal (the shutter) and each row is essentially continuously sensitive.

4.4.2 MAPS in the Tower-Jazz CMOS process

The 0.18 µm CMOS technology by Tower-Jazz has been selected for the implementation of the Pixel Chip for all layers of the new ITS. The main components of MAPS in in this process are shown in Fig. 25.

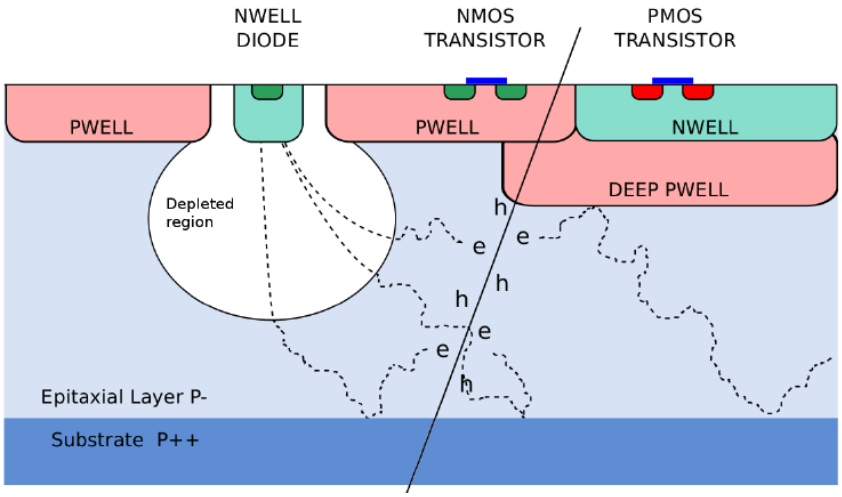

Figure 25: Schematic cross section of a MAPS pixel in the TowerJazz 0.18 µm imaging CMOS with the deep p-well feature.

SUBSTRATE: It is the lowest layer made of higly doped (p type), crystalline silicon with low resistivity. It provides mechanical stability and hosts all other structures.

EPITAXIAL LAYER: The epitaxial layer is grown on top of the substrate. This layer is lightly doped (p type) and forms the active volume of the detector where charge carriers are generated by the impinging particles. The active devices are embedded in this layer.

WELL IMPLANTATIONS: They are a bulk for the Field Effect Transistors. N-well and p-well implantations are used to integrate PMOS and NMOS transistors respectively.

DIFFUSION IMPLANTATIONS: They form the source and drain of the transistors. They have higer doping than the wells in which they are embedded into. P-type and N-type implantations are done for PMOS and NMOS respectively.

COLLECTION DIODE: The diode collects the charge generated in the epitaxial layer. The depletion region is formed at the junction between the diode n-well and the p-epitaxial layer.

METAL LINES: They connect the different silicon structures. They are generally made of aluminum or copper and embedded into silicon oxide, used as an insulator.

In the following, we discuss the main features that make this technology suitable, and in some respect unique, for the implementation of the ITS Pixel Chip.

- Due to the transistor feature size of 0.18 µm and a gate oxide thickness below 4 nm, it is expected that the CMOS process is substantially more robust to the total ionising dose than other technologies (such as AMS 0.35 µm).
- The technology allows for 6 metal lines. This, in addition to the small feature size, enables implementation of high density and low power digital circuits. This would reduce the area of the digital circuitry located at the periphery of the pixel matrix and would thus reduce the insensitive area of the pixel chip.
- It is possible to develop epitaxial layers with resistivity from 1 KΩcm to 6 KΩcm. This translates into bigger depletion area in the epitaxial layer which in turn would improve the signal to noise ratio of the sensor and, moreover, its resistance to non-ionizing radiation.
- Wafers with an epitaxial layer from 18 µm to 40 µm thickness can be produced; chips can be thinned down to 50 µm, which would significantly contribute to the reduction of material budget, an essential requirement for the ALICE ITS upgrade.
- One of the most important features offered by this technology is the availability of a deep p-well option in the CMOS process (see sec. 4.4). The use of a deep p-well in the region where the front-end electronics is foreseen circumvents the problem of the parasitic charge collection by n-wells necessary to accommodate PMOS transistors (see sec. 4.5). The n-wells that accommodate the PMOS transistors are fabricated on top of the deep p-well. The signal electrons are reflected by the electric potential at the junction between the epitaxial layer and the deep p-well and can be collected only by the sensing diode (see Fig. 25). Detailed description of the deep p-well implantation can be found in [57].
  ,
- The use of the stitching technology for the sensors production enables the manufacturing of die sizes up to a single die per 200 mm diameter wafer. However, for the ALICE ITS upgrade the collaboration will not take advantage of the stitching technology.

4.5 ALICE ITS PIXEL CHIP DEVELOPMENT

4.5.1 General requirements

The physics objectives and the design goals outlined in Chap. 3 have led to the following requirements for the pixel chip:

SILICON THICKNESS: Due to its contribution to the overall material budget of the ITS, it is desirable to make the chip as thin as possible. The minimal thickness is determined by the epitaxial layer height (nominal value is 18 µm, but thickness up to 40 µm is available) plus the height of the CMOS stack (around 10 µm). The fabrication of such a chip is done by thinning a standard-height wafer from the back. To remain with a safety margin, a thickness of 50 µm is required.

INTRINSIC SPATIAL RESOLUTION: The performances of the upgraded ITS and in particular its capability to separate secondary vertices of heavy flavour decays is determined by the impact parameter resolution. This is a convolution of the primary vertex resolution and the track pointing resolution and it is mainly determined by the performance of the inner layers. An intrinsic spatial resolution of 5 µm (30 µm) for the inner (outer) layers is required.

CHIP DIMENSIONS: The TowerJazz 0.18 µm CMOS technology allows for a maximum chip length of 30 mm in z-direction. A longer sensor would require the use of stitching technologies. The limitation of the chip width to 15 mm was motivated by geometrical considerations. For such width the deviation of the distance of each pixel from the nominal radius of each layer, the number of azimuthal segments and the deviation from an azimuthally vertical incidence angle are kept reasonably small. A chip size of 15 mm × 30 mm has consequently been chosen as baseline chip dimension.

For the Outer Layers it might turn out beneficial to have a differently sized chip. In particular, a rotated chip with a length of 30 mm in $r\phi$ direction is an interesting option since it would reduce the needed overlap of the Outer Layers. This would, however, require the development of a modified chip for the Outer Layers with respect to the one adopted for the Inner Layers. This is not pursued as a baseline solution, but is the kept as a future development option.

MAXIMUM DEAD AREA: To assure a hermetic detector configuration, overlaps of the chips are foreseen in $r\phi$ to allow for placing digital circuitry at their boundaries. This leads to localized increases of the material budget and thus needs to be minimized.

In z there is no such overlap foreseen and the dead area has a more stringent requirement. The performance simulations have been performed assuming a dead area of 2 mm in $r\phi$ and 100 µm in z-direction.

POWER DENSITY: The maximum tolerable material budget puts severe limitations on the amount of material that can be used for power distribution and detector cooling. The power density on the sensor has thus to be brought to a minimum and should not exceed 300 mW/cm^2 (100 mW/cm^2) for the inner layers (outer layers) in order to be compatible with the material budget requirement of 0.3% X0 and 0.8% X0, respectively.

INTEGRATION TIME: In order to cope with interaction rates of up to 50 kHz for Pb-Pb and up to 400 kHz for pp collisions, the maximum acceptable sensor integration time is about 30 µs in order to limit pile-up effects and a consequent loss of tracking efficiency.

DEAD TIME AT 50 KHZ INTERACTION RATE: A dead time of 10% at 50 kHz Pb-Pb interaction rate can be tolerated. On-chip memories and bandwidths must be dimensioned such that they can cope with the expected occupancy level.

DETECTION EFFICIENCY AND FAKE HIT RATE: A detection efficiency of at least 99% and a fake hit rate of not more than 10^{-5} per pixel and event are necessary to achieve the required track reconstruction performance.

RADIATION HARDNESS: In order to ensure full functionality especially for the ITS inner layers, the pixel detectors will have to be tolerant against the radiation levels expected for the innermost layer (radius of 22 mm) of 700 krad of Total Ionising Dose (TID) and a fluence of 10^{13} 1MeV neq/cm^2 of Non-Ionising Energy Loss (NIEL) including a safety factor of ten for a collected data set corresponding to 10 nb^{-1} Pb-Pb and 6pb^{-1} pp collisions.

4.5.2 First developments

The focus of the ALICE R&D is on assessing the radiation hardness and on studying the deep p-well approach in order to design circuits that minimize the power consumption and, consequently, affect the overall material budget.

An extensive R&D program is being carried out by the collaboration since 2012 to optimize the charge generation, collection and its transformation into an electrical signal. Different substrate materials have been considered: the resistivity and thickness of the epitaxial layer range from 1 kΩcm to 6 kΩcm and from 18 µm to 40 µm, respectively.

For the optimization of the pixel layout, an extensive set of different structures with different read-out circuits were developed and successfully characterized, both in terms of functionality and of radiation hardness. These prototypes include the MIMOSA-32/-34 and Explorer families. The latter is designed to allow reverse bias on the substrate, increasing the reverse voltage on the collection diode up to $-8\,V$ with respect to the typical values of $-0.8\,V$ to $-1.6\,V$ used in this technology. Details on the tests carried out on the MIMOSA-32 chip will be described in the following chapter.

4.5.3 Readout architectures

For the ALICE ITS upgrade development, the only information of relevance from the pixel chip is whether or not a particle is crossing a pixel. This information is obtained by applying a threshold to the analogue signal of a collection node. Where and how this is done is where the proposed architectures differ the most.

At present, three different architecture design lines are under development. Two (MISTRAL and ASTRAL) are being developed at IPHC of Strasbourg and are both based on the rolling shutter readout architecture. MISTRAL (which derives from the ULTIMATE chip designed for and operated in the STAR-PXL detector at RHIC [58]) is equipped with column-level discriminators allowing simultaneous two-rows read-out and a power consumption of about $300\,mW/cm^2$; in ASTRAL, taking advantage of the Tower-Jazz technology, the signal discrimination is at pixel level, thus reducing the peripheral circuitry dimensions; the readout frequency is also doubled and the power consumption is reduced to about $150\,mW/cm^2$ since the column drivers now drive digital signals, which requires less power.

When the digital information is available in the pixel itself, one may consider other readout schemes as well. One example is a data-driven read-out in which the digital outputs of the pixels are fed into an encoder circuit that generates directly the address of a hit pixel. This can, in turn, be used to reset this pixel and go to the next valid one; the procedure is iterated until all pixels are read out. The big advantage, in addition to the low power consumption, is the fast read-out time. This approach is followed by the ALPIDE development, pursued by a collaboration formed by CCNU (Wuhan, China), CERN, INFN (Italy), NIKHEF (The Netherlands) and Yonsei (South Korea).

It is important to note that the way the read-out is performed in the rolling-shutter architecture implies that the sensor is always integrating for a full shutter period, which typically ranges between $30\,\mu s$ (MISTRAL) and $20\,\mu s$ (ASTRAL). Signals from all events within this time are integrated, which leads to pile-up in case of large bunch-crossing rates. For the ALPIDE chip, in its default mode of operation

a global strobe signal is used to capture the output of the comparator front end into a local memory. The effective integration time is about 4 µs and is given by the shaping time of the front end.

First full scales prototypes (FSSB for MISTRAL and p-ALPIDEfs for the ALPIDE architecture) have been received in Spring 2014 and are currently under test with very promising results. In the Chap.6 the development of a telescope setup to perform a comparative study of both the full scale sensors will be described.

5 MIMOSA32 CHARACTERIZATION MEASUREMENTS

Contents

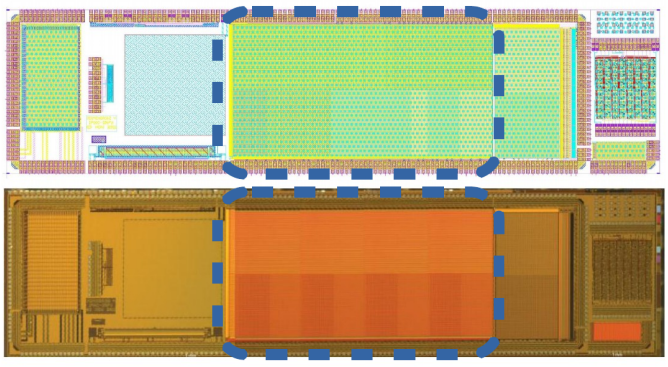

Figure 26: Image of MIMOSA32 - The 32 pixel matrices are found in area marked by a dashed blue line. Each matrix has 16 columns and 64 rows.

The *"Minimum Ionising Particle MOS Active Pixel Sensor"* (MIMOSA) has been developed by the Institut Pluridisciplinaire Hubert Curien (IPHC) from Strasbourg.

Since 1999, approximately 40 designs (either prototype or full scale) have been produced implementing many different architectural and pixel cell solutions as well as different CMOS processes, with different epitaxial and substrate layer thicknesses and resistivities. MIMOSA-32 is the first chip whose properties have been studied in the framework of the ALICE ITS upgrade.

5.1 CHIP OVERVIEW

MIMOSA 32 is a prototype chip consisting of pixel structures produced using TowerJazz 0.18 µm CMOS process. The properties of these structures were studied, in particular their charge collection properties, to validate the technology for the ALICE ITS Upgrade programme.

MIMOSA32 includes traditional MAPS structures with NMOS transistors and also structures with a deep p-well implementation. The pixel circuits with the deep p-well implementation does not include PMOS transistors but the motivation is to study the effects of this deep p-well, if its presence produces any effects and if it disturbs the performance.

The chip features an 18 µm epitaxial layer with high resistivity $\rho = 30\,\mathrm{k\Omega cm}$. Total thickness of the chip, including the substrate is approximatively 450 µm.

The chip (see Fig. 26) consists of five blocks aimed at studying different aspects of CMOS sensors like discriminators, steering circuits etc. The different pixel structures are located in the central area, they consist of 32 matrices of pixels with different collecting diode sizes and transistor implementations, and their study is the object of this work.

There are 22 matrices where the sensing diode is connected to a Source Follower (SF), structures are both 3T and 2T (see Section 4.4.1), in each matrix pixels are distributed in 16 columns and 64 rows. The remaining ten matrices contain an additional preamplification chain.

In Tab. 4 the characteristics of the 3T structures whose characterization results will be presented in the next sections are summarized. They differ for the shape and area of the collection diode and the presence of the Deep Pwell and its size. Most of these structures are equipped with *Enclose Layout Transistors (ELT)* [59] to improve radiation tolerance.

5.1.1 MIMOSA32 readout

MIMOSA-32 has a 16-channel analogue output bus so an entire row of 16 pixels is read out in one clock cycle.

Structure	Collection Diode		Characteristics
P2	Octagonal	$\sim 11\,\mu m^2$	ELT
P4	Octagonal	$\sim 11\,\mu m^2$	
P7	Square	$\sim 20\,\mu m^2$	ELT
P8	Octagonal	$\sim 11\,\mu m^2$	ELT, Small Deep PWell
P9	Octagonal	$\sim 11\,\mu m^2$	ELT, Medium Deep PWell
P10	Octagonal	$\sim 11\,\mu m^2$	ELT, Large Deep PWell

Table 4: Main characteristics of MIMOSA32 structures

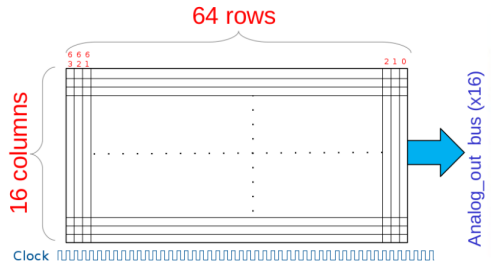

Figure 27: Rolling shutter readout scheme. Pixel matrix is read row by row. One row is read in one clock cycle and the entire matrix in 64 cycles. As soon as the readout of the last row is completed, readout of first row is initiated.

Pixels in a column are multiplexed on a single output line. In other words, pixels from same row are read out in parallel and those in the same column in series (see Fig. 27). A pixel matrix is read out continuously row by row using the *rolling shutter* technique described in Sec. 4.4.1.

MIMOSA32 is operated by a 2 MHz clock which means that a row is read out in 500 ns, while the entire matrix (of 64 rows) in 32 µs.

A *Frame* represent the readout of an entire matrix. It contains information about the output voltage of every pixel in the matrix with a time delay of 500 ns between two consecutive rows. The next Frame starts immediately after the previous has finished. Every pixel is read only once in a Frame so 32 µs pass between two consecutive readouts of a pixel. This time is called *integration time* since the sensing diode integrates all the charge it collects in that period.

5.1.2 Correlated double sampling

The "Correlated Double Sampling" (CDS) is a method for determining the charge integrated by a pixel during the integration time. It consists of the difference of two consecutive readouts of either a single pixel or a Frame (16×64 pixels).

$$\mathrm{CDS} = \mathrm{Frame}_n - \mathrm{Frame}_{n-1} \tag{16}$$

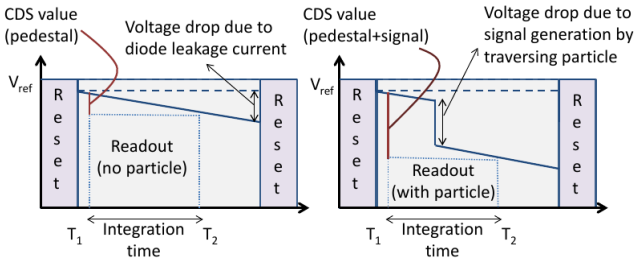

Figure 28: Correlated double sampling

Fig 28 illustrates the principle of operation of the CDS technique in the case of a 3T structure. During the period of time between two resets of the voltage applied to the collecting diode the pixel is read twice (the first time at T_1, the second at T_2). The difference between the two values gives the CDS of that pixel. If no particle has crossed the detector between T_1 and T_2 the value of the CDS is mainly due to the drop of the voltage on the collecting diode caused by the leakage current. Otherwise on top of this effect it is dominant the voltage drop due to the generation of a signal by the traversing particle.

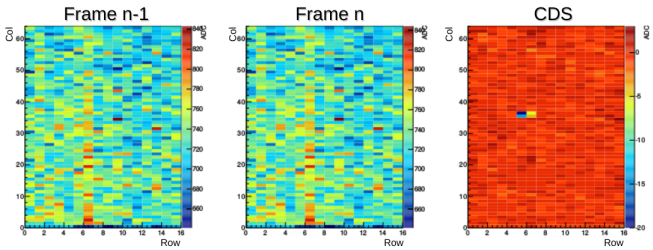

Figure 29: Example of a CDS evaluated for a structure of MIMOSA32 exposed to an ^{55}Fe source. Left plot shows a readout of the complete matrix (charge collected is converted in ADC counts), the central plot shows a complete readout of the matrix after the integration time. The right plot is the difference between the two subsequent frame.

Fig. 29 shows an example of CDS for a structure of MIMOSA32 exposed to an ^{55}Fe source (see sec. 5.3.1). It is clearly visible in the CDS the effect in some pixels of the sensor on the output due to the energy deposited by an X-ray emitted by the source.

5.2 DATA ACQUISITION SYSTEM

Fig. 30b shows the Data Acquisition System of MIMOSA32, developed by the University and INFN (Instituto Nazionale di Fisica Nucleare) of Cagliari. The system can be split in the following parts :

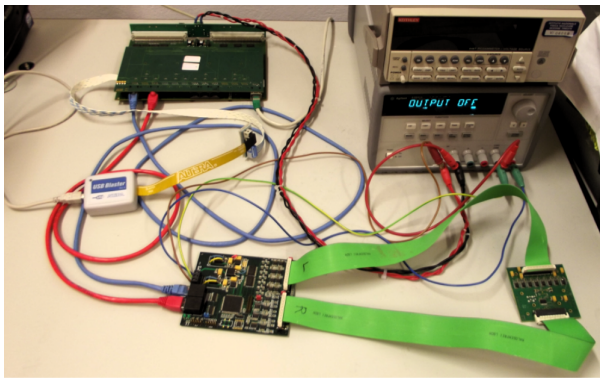

(a) Photo of the readout system. Top left: ZRC. Bottom left: Auxiliary Card. Bottom right: Proximity Card.

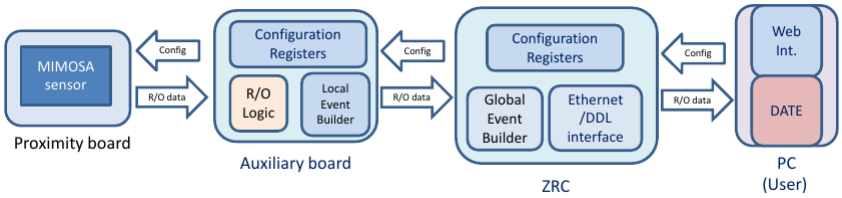

(b) Readout system schematic for MIMOSA32. Principal tasks of each card composing the readout system

Figure 30: Data Acquistion System for MIMOSA32 readout developed by the University and INFN (Instituto Nazionale di Fisica Nucleare) of Cagliari

PROXIMITY CARD with wire-bonded MIMOSA32 and first amplification stage. There are eight amplifiers with two channels each, that is all sixteen MIMOSA-32 analogue output channels are amplified in parallel. It has two flat cable connectors, one for power and steering signals and one for output signals, both connected to the Auxiliary Card.

AUXILIARY CARD is responsible for the readout of MIMOSA32. Analogue output signals coming from amplifiers on the Proximity Card pass trough a second amplification stage (again eight amplifiers with two channels each) and are digitized by sixteen 10-bit ADCs (one per channel). Digital potentiometers provide adjustable voltage levels (i.e. used as reference voltage of ADCs). Steering signals for MIMOSA-32 are given by a programmable FPGA.

The FPGA calculates the CDS values; only if any of them is above a pre-set threshold (usually about 20 ADC), data are recorded, thus giving the possibility to have a sort of *"internal trigger"*. A set of output pins provides access to various signals (e.g. MIMOSA-32 clock) sent or received by the FPGA. The Auxiliary Card requires +5 V, -5 V and ground, and has two

RJ45 connectors for a two-way communication with the ZDC Readout Card.

ZDC READOUT CARD is a general purpose card developed for the data acquisition system of the ALICE Zero Degree Calorimeter [60] adapted for the readout of the MIMOSA32. It receives the digitized data from the Auxiliary Card, and sends them to a PC. Different mezzanine cards can be connected to the ZRC according to the needs of the application. It is controlled by another programmable FPGA. Interface mezzanine contains connectors for up to four Auxiliary Cards and an Ethernet interface (serial to Ethernet converter called XPort [61]) used for configuring the readout system and sending data to a PC. Data can also be sent to a PC using an optical fibre, and in this case a specialised mezzanine is needed. The last mezzanine is a NIM Trigger Card. ZRC requires +5 V power supply.

5.3 LABORATORY MEASUREMENTS WITH ^{55}Fe SOURCE

The purpose of the laboratory tests using a radioactive source is to measure the following sensor parameters:

- Equivalent Noise Charge (ENC)
- Charge Collection Efficiency (CCE)

The ENC of a sensor is expressed in terms of number of electrons. The analog data from the pixels are readout in ADC units. A calibration procedure is needed to quantify the ADC units in electrons to express the ENC. This is generally done using a radioactive source with a known spectrum.

In this case measurements have been performered using an Fe-55 source.

5.3.1 ^{55}Fe emissions

$^{55}_{26}Fe_{29}$ disintegrates by electron capture with half life of $T_{1/2} = 2.747\,y$. Particles produced by its decay, along with their energies and rates normalized to 100 disintegrations are reported in Tab. 5.

A $10\,keV$ electron has a range of $2.88\,g/cm^2$ [63] in air, that is $0.24\,cm$ which is smaller than the usual distance between the source and the detector (some centimeters). The emission probability of a $126\,keV$ γ-ray is eight orders of magnitude lower than the emissions of X-rays, therefore its contribution to the measured spectrum is negligible.

Attenuation coefficients in air for 1.0, 5.9 and $6.5\,keV$ X-rays are 3.58×10^3, 23.7 and $17.7\,cm^2/g$ respectively [64]. For distances be-

	Energy [keV]	Emissions per 100 disint.
Auger Electrons	0.47 - 0.67	140.2 (8)
	4.95 - 6.53	60.1 (5)
X-rays	0.56 - 0.72	0.524 (21)
	5.888	8.45 (14)
	5.899	16.57 (27)
	6.490	3.40 (7)
	6.535	
γ	125.959	$1.3\,(1) \times 10^{-7}$

Table 5: ^{55}Fe emissions [62]. Numbers in parenthesis are errors on the last digit(s) of the preceding value.

tween the source and detector of about few centimetres, all emitted X-rays can reach the detector, but the flux of the X-rays with the lowest energies is significantly reduced.

Intrinsic energy resolution is given by Eq. (17). [55]

$$R = 2.35\sqrt{\frac{Fw}{E}} \tag{17}$$

where F is the Fano factor in silicon ($F \approx 0.116$ for 5.895 keV [65]), w the energy required to excite an e-h pair ($3.6\,eV$) and E the energy deposited by a photoelectron. From equation 5.1 we obtain $R \approx 2\% (\approx 120\,eV)$ for energies between 5.9 and 6.5 keV. Therefore, 5.888 and 5.899 keV (6.490 and 6.535 keV) X-rays can't be resolved. In conclusion, we expect to see only two peaks from the photoelectric absorption of 5.9 and 6.5 keV photons in silicon.

Since on average the energy required to produce an e-h pair is 3.6 eV, the 5.9 keV and 6.5 keV photoelectrons will create about ≈ 1640 and ≈ 1800 e-h pairs respectively [66] .

5.3.2 Seed Spectrum

First, a pedestal run without the source is performed. Each event contains the data from two consecutive frames. Each frame corresponds to the entire pixel matrix which is readout row by row. The difference between the two consecutive readings for each event are taken (correlated double sampling). Then the average of the CDS value for each pixel over all events is mapped. This gives the pedestal value in ADC units for each pixel. Left panel of Fig. 31a shows an example pedestal map for P7 structure (see Tab.4). The standard deviation of the pedestal distribution for each pixel gives the noise value in ADC units for each pixel. Fig. 31b and Fig. 31c show the noise map for the same matrix and the Noise distribution. The average

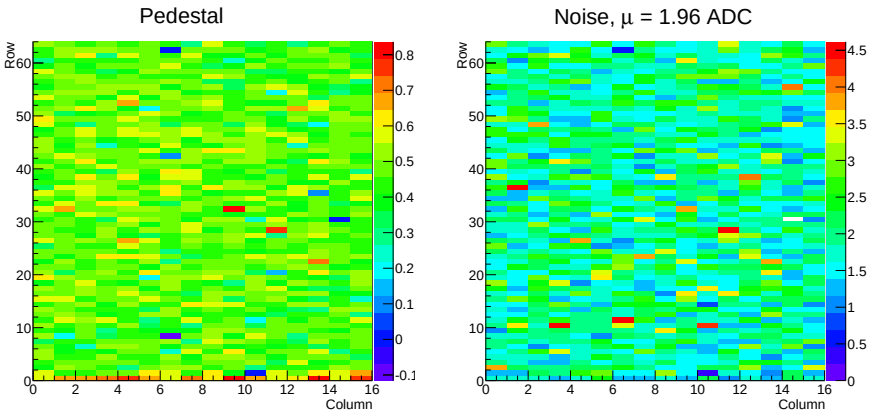

(a) Pedestal map. Average of the CDS value for each pixel over the events in a run without source.

(b) Noise Map. Standard deviation of the pedestal distribution. The noise of the entire structure is considered as the average of the noise in each pixels (indicated in the plot title label).

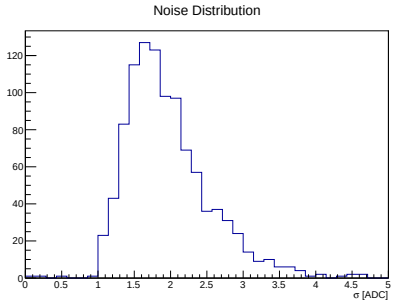

(c) Noise Distribution. Distribution of the standard deviation of the pedestal distribution.

Figure 31: Pedestal (Fig. 31a), Noise (Fig. 31b) map and Noise Distribution of MIMOSA32 P7 structure (see Tab.4).

value of the noise of all the pixels is considered as the noise of the entire matrix. In this case, the noise of the P7 matrix is 1.96 ADC.

Next, a run with the Fe-55 source is performed. The CDS data is computed from the raw data. The pedestal value for each pixel (from the previous pedestal run) is subtracted from the CDS value of the corresponding pixel. Then, the pixel with the highest signal is searched. If the signal is above a certain threshold, then the pixel is defined as the seed pixel. In this case, the threshold value of each pixel is five times the noise value for that particular pixel.

The search for the seed pixel excludes the borders of the matrix. The borders consist of first two and last two rows and columns of the matrix. This is done to accomodate potential candidates for a cluster of neighbouring pixels around a seed. After the seed pixel is found, a matrix of 5x5 pixels is considered around the seed pixel

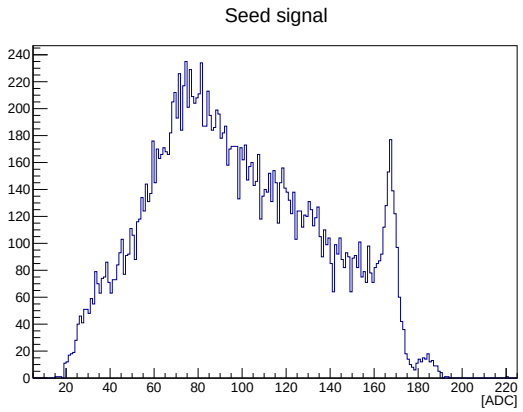

(a) Distribution of charge in the seed pixel over events. Seed pixels are those which have the ratio signal over noise greater than 5.

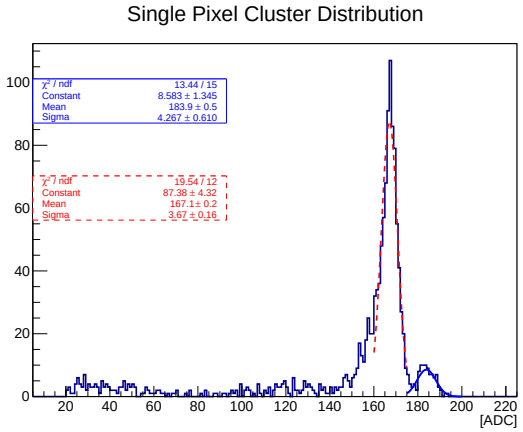

(b) Distribution of charge for single pixel cluster.

Figure 32: Seed spectrum (Fig. 32a) and single pixel distribution (Fig. 32b) obtained with MIMOSA32 structure P2 (see Tab.4) exposed to ^{55}Fe source.

to search for clusters. Excluding the two outer rows and columns from the searching region for the seed excludes the possibility to have incomplete clusters. A neighbouring pixel of the seed having a signal above a certain threshold is considered as a cluster pixel. In this case, the threshold selected for a pixel is three times the noise for that pixel.

After pixels have been associated to the cluster, the map is scanned again to search for others seed pixels and the clustering algorithm is repeated. Then the whole procedure is repeated for all the events.

The distribution of charge in the seed pixel over all events gives the seed spectrum.

Fig. 32a shows the seed spectrum obtained with MIMOSA32 structure P2 (see Tab.4) exposed to ^{55}Fe source. The lowest possible ADC value is user defined by a hardware threshold of the readout system (see Sec. 5.2).

The different peaks in the Fe-55 spectrum can be explained as follows. The X-ray photons from the Fe-55 source generate electron-hole pairs in the epitaxial layer. The charge carriers are generated close to the interaction point. The electrons diffuse randomly in the undepleted region of the epitaxial layer and are reflected from the substrate and the p-wells, which results in the movement of a part of these electrons into the neighboring pixels.

Thus there is a charge spread and a cluster of charge is formed. In these events, only a part of the signal generated is collected by the seed pixel. This corresponds to the broad peak around 80 ADC counts in Fig. 32a.

When the photons interact at points very close to the depletion region of the sensing diode, the generated electrons are collected entirely by the sensing diode, resulting in a single-pixel cluster. In Fig. 32a, this is visible in the extreme right of the spectrum where there are two peaks at ≈ 170 and ≈ 190 ADC counts.

In these events, the seed pixel collects the entire charge generated. The smaller peak around 190 ADC counts corresponds to 6.5 keV peak of the iron spectrum. The larger peak at around 170 ADC counts corresponds to 5.9 keV peak. This peak is used as the calibration peak and is used to convert the ADC counts to electrons.

Fig. 32b shows the single-pixel cluster distribution, extracted from the seed spectrum. In this case the region at low ADC value is completely empty, only the two peaks corresponding to the two X-ray emissions of the source are present.

5.3.3 Equivalent Noise Charge (ENC)

In order to compare noise of different chips and structures it is necessary to express it in a quantity which does not depend on the specific setting used (e.g. the voltage reference for the ADC). For this reason the value of the noise in term of ADC it is usually converted in number of electrons- holes pairs generated in the sensor. As seen in Sec. 5.3.1 a photoelectrons of $5.9\,keV$ creates on average ≈ 1640 e-h pairs, this means that we can find a relation between ADC and number of electrons generated:

$$N_{e^-} : N_{ADC} = 1640 : x_{Peak} \tag{18}$$

where N_{ADC} is a value expressed in ADCs, N_{e^-} is the correspondent value expressed in numeber of generated electrons and x_{Peak} is the position in ADC values of the 5.9 keV peak evaluated fitting with a gaussian the seed spectrum [1].

1 The process of charge collection is not Gaussian, as it is not possible to collect more charge than what created, but only to lose part of it. As a consequence, in a perfect system the peak should have a specular Poisson shape. However the noise superimposed to the charge collection process is Gaussian, and being the charge collected

$5.9keV$ Seed Peak Position	167.1 ± 0.2
Conversion Factor $[e/ADC]$	$9,81$
Noise $[ADC]$	2.74
ENC $[e]$	26.88
$5.9keV$ Cluster Peak Position	164.1 ± 0.1
CCE	$98 \pm 0.1\%$

Table 6: Conversion factor from ADC to number of generated electrons, Equivalent Noise Charge and Charge Collection Efficiency obtained for structure P2.

With this conversion factor it is possible to express the noise of the structure in term of ENC, for the example given in Fig. 32b the values obtained are indicated in Tab. 6

5.3.4 Cluster signal and Charge Collection Efficiency (CCE)

For each identified cluster the total charge in the cluster (including the seed) is computed for all events, giving the cluster signal distribution shown in Fig. 33 This distribution shows how summing together all the charge collected in the cluster the broad peak at low ADC values disappears and all the signal is concentrated in the region of ADC corresponding to the Fe-55 emissions.

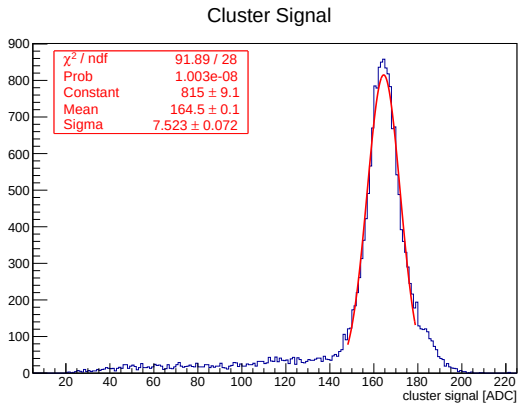

Figure 33: Cluster signal distribution

The charge collection efficiency is given by the ratio between the numer of electrons detected in the sensor (i.e. the number of electrons collected in the cluster) and the number of expected eletrons.

large (1600 e-), the Poissonian behavior is negligible respect to the noise Gaussian one, rendering the Gaussian fitting effective for any practical purpose.

$$CCE = \frac{e^-_{meas}}{e^-_{exp}} = \frac{\mu_{clust}[e^-]}{1640} = \frac{\frac{1640}{\mu_{peak}[ADC]}\mu_{clust}[ADC]}{1640} = \frac{\mu_{clust}[ADC]}{\mu_{peak}[ADC]} \tag{19}$$

where $\mu_{clust}[e]$ is the charge collected in the cluster expressed in number of electrons, $\mu_{clust}[ADC]$ is the charge collected in the cluster expressed in ADC value and $\mu_{peak}[ADC]$ is the position of the $5.9\ keV$ peak in the seed spectrum.

The value of CCE for the reported example is given in Tab. 6

5.3.5 Cluster Multiplicity

Fig. 34 shows the cluster multiplicity distribution obtained with structure P2 exposed to ^{55}Fe source. The mean of this distribution can be used to quantify the charge spread among the neighbour pixels.

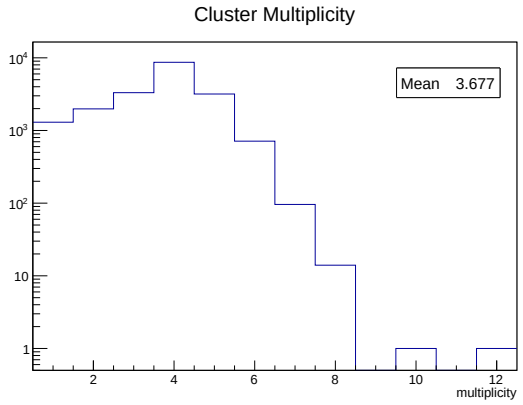

Figure 34: Cluster multiplicity distribution obtained with MIMOSA32 structure P2 (see Tab.4) exposed to ^{55}Fe source.

Fig. 35 shows the the contributions to the seed spectrum (see Fig. 32b) of seed pixel belonging to clusters with different multiplicities. As can be shown in Fig. 35b the higher is the multiplicity of the cluster the lower is the seed charge value.

5.3.6 Different structures comparision

Fig. 36 shows the comparison of the MIMOSA32 matrices which are mentioned in Tab 4. The P4 matrix consists of square pixels of $20\,\mu m$ pitch, based on a 3T structure with an octagonal collection diode of area $10\,\mu m^2$. The P2 matrix is similar to P6, but has an Enclosed Layout Transistor (ELT) structure [59] designed to improve radiation hardness. The matrices P8 and P10 have the same collection diode but are equipped with a deep p-well implemented along with

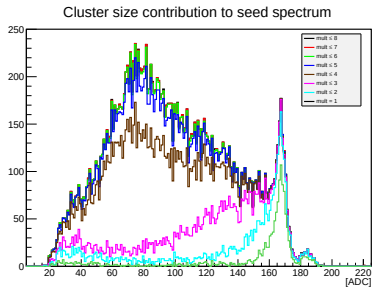

(a) Seed spectrum obtained with the charge of seed belonging to clusters up to a certain multiplicity

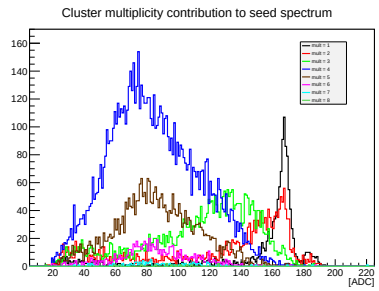

(b) Seed spectrum obtained with the charge of seed belonging to clusters with defined multiplicity

Figure 35: Contribution to Seed Spectrum of MIMOSA32 P2 structure exposed to ^{55}Fe source of seed belonging to clusters with different multiplicities

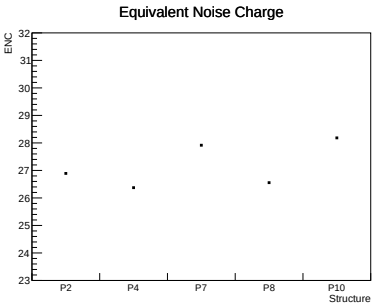

(a) Equivalent noise charge

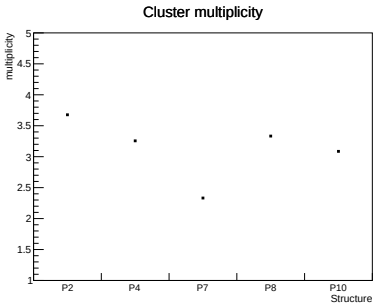

(b) Cluster Multiplicity

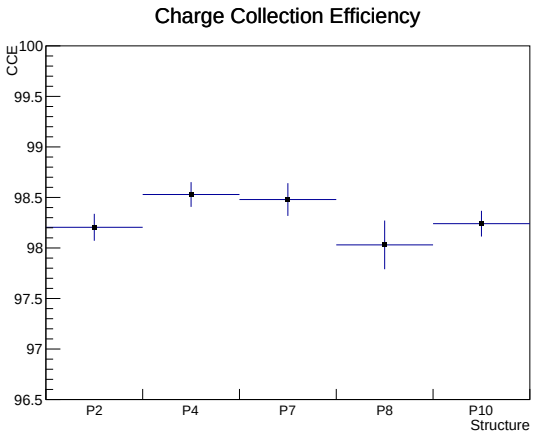

(c) Charge Collection Efficiency

Figure 36: Comparision of the results obtained for different structures in terms of ENC (Fig. 36a), cluster multiplicity (Fig. 36b) and CCE (Fig. 36c)

a traditional MAPS design with NMOS transistors. Matrix P7 has a square diode of area 20 μm^2 instead of an octagonal one.

The Fig. 36a show the comparison of the ENCs. All the matrices have comparable ENCs around 27 electrons. The CCE (Fig. 36c) of all the matrices is above 98%. Also the mean cluster multiplicity (Fig. 36b) has comparable values except for structure P7, which indeed has a larger collecting diode.

All the five structures tested have satisfactory charge collection properties, which shows that the technology is promising for further optimization of the pixel properties in future prototypes. The results show that the presence of a deep p-well in the pixels (which have a traditional design with NMOS transistors) does not affect the performance of the pixel and maintain similar charge collection properties like the pixels without the deep p-well. Thus the deep p-well in a pixel does not introduce any degradation in performance. This validates the use of the deep p-well option in future prototypes for implementing full CMOS in-pixel circuits thereby allowing sophisticated in-pixel signal processing circuits.

5.3.7 Dependence of the output on the voltage applied to the collection diode

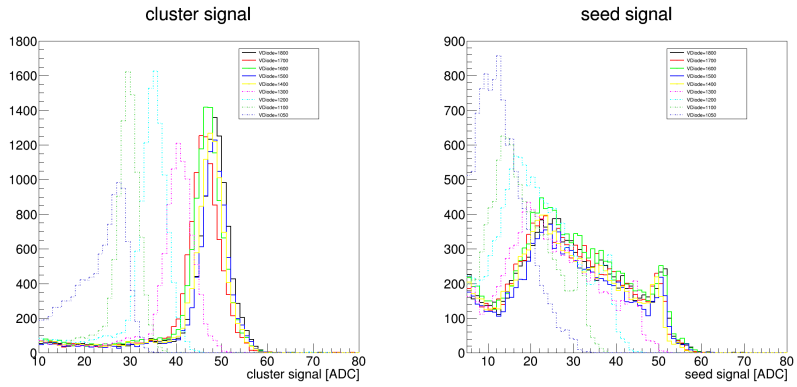

(a) Cluster charge distribution **(b)** Seed spectrum

Figure 37: Seed spectrum (Fig. 37b) and Cluster signal (Fig. 37a) for different values of the voltage applied to the collection diode.

Fig. 37 shows the seed spectrum (Fig. 37b) and the cluster signal distribution (Fig. 37a) for values of the voltage applied to the collection diode (V_{diode}) ranging from 1050 mV to 1800 mV.

Decreasing the voltage applied to the collection diode, since the diode is inversely polarized, decreases the depletion zone in the epitaxial layer. This means that for low values of V_{diode} the collection mechanism of the charge is mainly due to diffusion. In these conditions charge spread among neighbouring pixels is higher, leading to a seed spectrum with higher contributions at low ADC values.

When electrons diffuse randomly their path in the silicon is longer and this increases the probability of recombination. This can be observed in the seed and cluster spectrum since the decrease of V_{diode} moves the distributions to lower ADC value (meaning that a lower amount of charge has been collected).

For values of $V_{diode} > 1400\,mV$ no significant modifications of the distributions can be observed meaning that the maximum possible region of the epitaxial layer has been depleted.

5.3.8 Calibration in Energy

Exploiting the known relation between the energy deposited and the two peaks of the single pixel cluster signal distribution (Fig. 32b) it is possible to estimate the relation between energy deposited and signal output.

We expect indeed the relationship between the output of the sensor and the energy deposited to be linear. Therefore by matching the position of the two peaks of the single pixel cluster signal distribution (as mean of a gaussian distribution) with the corresponding energy emission of the ^{55}Fe source and by imposing that without any energy deposited in the sensor the ADC output should be 0, it is possible to interpolate and find the relationship between ADC values and energy deposited in the sensor.

Fig. 38 shows this linear interpolation for structure P2 of MIMOSA32, in this case the relation obtained is

$$E[keV] = p_0 + p_1 \cdot x[ADC] \tag{20}$$

where the two fit parameters p_0 and p_1 are shown in Tab. 7

p_0 [keV]	p_1 [keV/ADC]
2 ± 5	28.0 ± 0.9

Table 7: Fit parameters for ADC to Energy conversion

Similar results have been obtained by the INFN Catania group [67] exploiting the X-ray emissions of different sources (see Tab. 8), the linear relation between the output of the sensor and the deposited energy is well confirmed up to 32 keV.

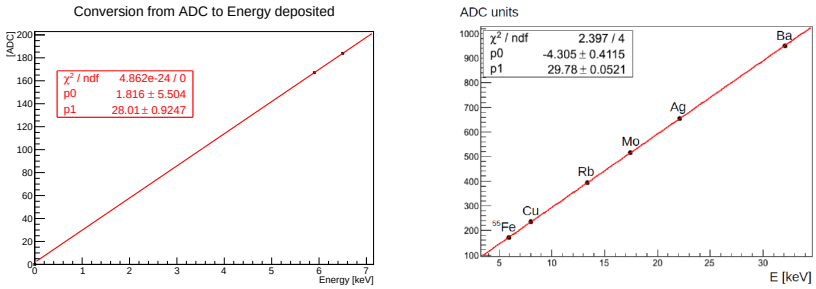

(a) Results obtained exploting the two X-ray emissions of ^{55}Fe source

(b) Results obtained by the INFN Catania group using different emitting sources (see Tab. 8)

Figure 38: Linear relation between energy deposited and ADC output of the sensor for MIMOSA32 structure P2

Source	Emission Energy [keV]
^{55}Fe	5.9
Cu	8.04
Rb	13.37
Mo	17.44
Ag	22.10
Ba	32.06

Table 8: Emission energy of source used by INFN Catania group to test the linearity between output of the sensor and the energy deposited in the sensor

5.4 TESTBEAM MEASUREMENTS

MIMOSA32 prototypes were also tested with 4 GeV electrons beam at DESY facility (in Hamburg, GE) in March and June 2013, Fig. 39 shows the setup used during the testbeam.

In this case the sensors performance is tested with minimum ionizing particles. The particles passing through the epitaxial layer generate electron-hole pairs along their trajectory. The electrons then move along the sensor and are collected by the collection diode.

The sensor parameters which are measured are:

- Signal to noise ratio (SNR)
- Detection Efficiency

5.4.1 Signal to noise ratio

The data acquisition and data treatment procedure for the beam tests are similar to that of the Fe-55 source. The noise of the matrix is found from a pedestal run. Then a beam run is performed and the

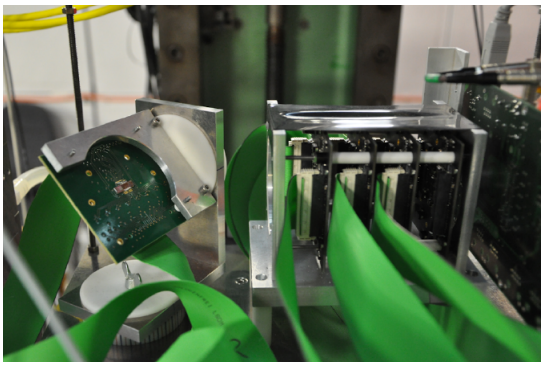

Figure 39: MIMOSA32 testbeam setup at DESY facility in Hamburg. On the right a stack of three sensors is shown, the stack has been used to evaluate the detection efficiency of MIMOSA32. On the left part of the picture is visible a sensor mounted on a rotating support in order to study the relation of the signal with the variation of the angle.

data are analyzed to find the seed pixels and the clusters. The seed signal distribution for MIPs obtained with MIMOSA32 P2 structure is shown in Fig. 40a, the distribution is fitted with a convolution of a landau distribution and a gaussian distribution. Indeed the MIPs passing through the sensor lose an amount of energy whose distribution is expected to be a landau but, as we have seen in sec. 5.3.2, not all the charge generated is collected by the seed pixel. The convolution of the landau and the gaussian distribution is meant to take into account this spread effect of the generated charge.

The cluster signal is built also in this case summing the charge of the seed neighbour pixels which have a signal 3 times greater their noise. The cluster signal distribution for P2 structure is shown in Fig. 40b.

The seed and the cluster signal can then be divided by their noise to give the *Signal to Noise Ratio (SNR)* distributions. The SNR of the seed and the cluster signal for P2 structure are shown in Fig. 40c and Fig. 40d. They are interpolated with a Landau distribution. The Most Probable Value (MPV) of the cluster SNR distribution is used to quote the SNR of the pixel matrix.

To test the degradation of MIMOSA32 performance some chips were subjected to irradiation process before being bonded on test board. Fig. 40d shows the cluster SNR distributions of a non irradiated chip and of a sensor irradiated with protons (irradiation level $2.6\,10^{13}$ protons). It can be noticed that for the irradiated chip the distribution moves to lower values of the ratio signal to noise.

Irradiated chip

In this section some features of the irradiated chip will be discussed and compared to the ones of the non irradiated. The chip here consid-

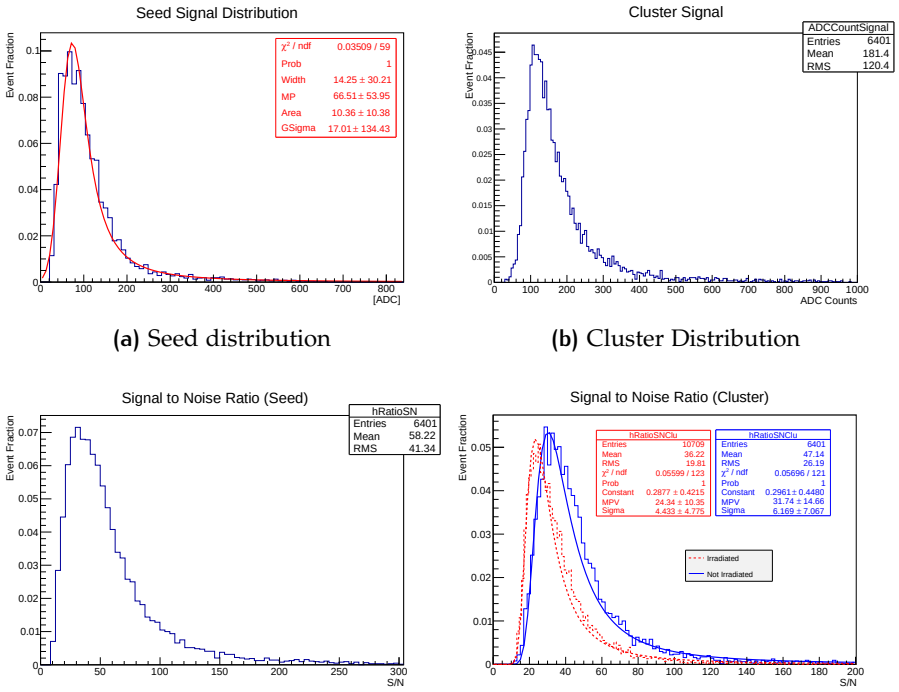

(a) Seed distribution

(b) Cluster Distribution

(c) Seed Signal to Noise Ratio distribution.

(d) Cluster Signal to Noise Ratio. Comparision between irradiated (red dotted line) and not irradiated (blue solid line) chip.

Figure 40: MIMOSA32 structure P2 Seed (Fig. 40a), Cluster (Fig. 40b) and SNR (Fig. 40c and Fig. 40d) distributions. Data refer to a testbeam with 4 GeV electrons performed at DESY facility in Hamburg

ered is irradiated with protons with an irradiation level of $2.6 \cdot 10^{13}$ protons, the aim of this process is to validate the technology for radiation hardness. The irradiation of the chip causes:

- increase of the leakage current and a consequent variation of the pedestal distribution
- increase of the noise level
- lowering of the signal and, as a consequence, lowering of the signal to noise ratio

Fig. 40 shows the distribution of the MIMOSA32 P2 structure CDS in a pedestal run for an irradiated (Fig. 46a) and a not irradiated (Fig. 46b) sensor. The increase of the leakage current causes a lowering of the pedestal, this can be observed since the distribution of the CDS for not irradiated chip is usually nearly centered at 0 ADC while it is extremely lower for the irradiated ones (as visible in Fig. 41).

Fig. 42 shows a comparison of the MPVs of the SNR distribution for different structures of MIMOSA32. A degradation of the SNR is

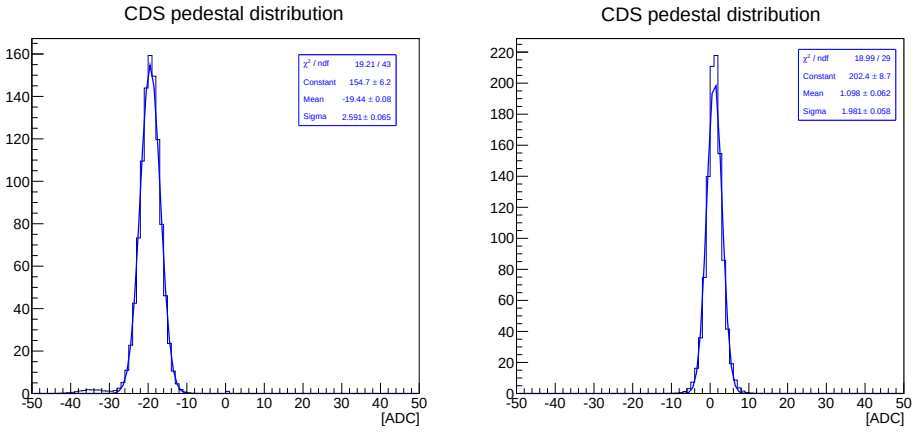

(a) Irradiated chip **(b)** Not irradiated chip

Figure 41: CDS distribution nof MIMOSA32 P2 structure in a pedestal run for an irradiated (Fig.46a) and a not irradiated (Fig.46b)

visible for all structures but the signal remains more than 20 times the noise even after the irradiation assuring a satisfying signal recognition capability.

Structures equipped with deep pwell implementations (P8, P9) do not differ in their behaviour from the others structures confirming that their presence do not affect pixel performance even after irradiation.

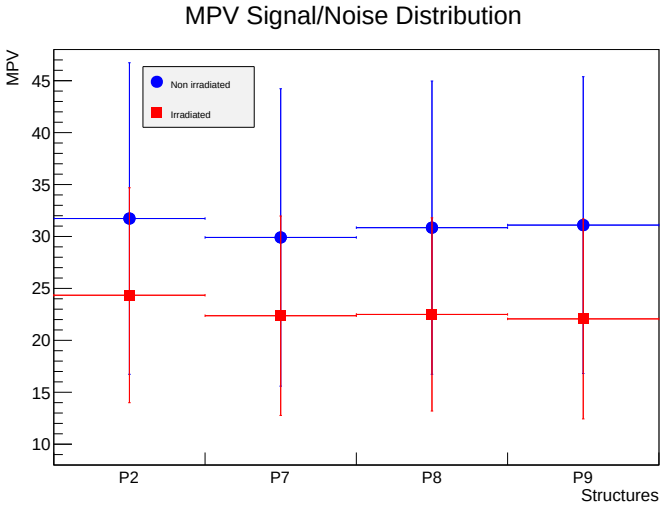

Figure 42: Comparision of the cluster SNR for different structures. Both results concerning a not irradiated (blu circle) sensor and a sensor irradiated with protons (red square) are shown.

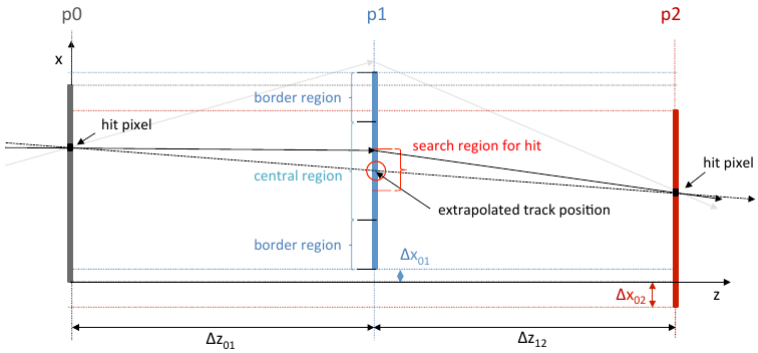

Figure 43: Scheme of the strategy used for the hit-track association in the detection efficiency analysis

5.4.2 Detection efficiency

The detection efficiency is measured with the use of a beam telescope. The sensor under test (DUT) is placed between the planes of a telescope. First tracks are reconstructed from the hits in the planes of the telescope, then hits are searched in the sensor under test at the intersection points with the tracks. The ratio between the hits detected in the sensor to the number of reconstructed tracks in the telescope planes gives the detection efficiency of the sensor. A custom telescope using three planes of MIMOSA32 sensors was used with the middle plane as the device under test.

Fig. 43 shows a scheme of the strategy used to associate the hit on the device under test to the reference track. Only events with a single hit in the first plane are considered. These hits are then associated with the hits in the last plane and tracks are reconstructed. A cuts of 10 times the noise and 3 times the noise are considered for the seed pixel and the neighbouring pixels of the seed in the cluster. Hits are then searched in the middle plane corresponding to these tracks, in a zone of 5×5 pixels around the reconstructed track. The ratio of the number of these hits found in the middle plane to the number of reconstructed tracks gives the detection efficiency.

Fig. 44 shows the detection efficiency of structures P2 and P6 as a function of the cut on the seed of the DUT plane. The detection efficiency for both the structures shows a plateau above 98 % for cuts on the seed lower than 10 times the noise.

5.4.3 Inclination angle

Some runs varying the inclination of the chip with respect to the beam direction were made. A different inclination of the sensor causes the variation of the particle path length in the sensor and, therefore, a variation in the amount of energy deposited by the in-

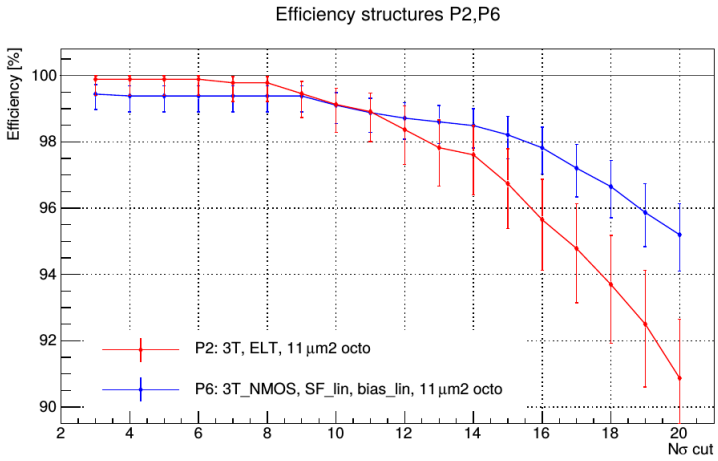

Figure 44: MIMOSA32 Detection efficiency for structure P2 and P6 as a function on the cut of the seed of the DUT plane

coming beam. In particular the amount of energy deposited in the sensor is expected to be proportional to the path length. The sensor was inclined in the azimuthal direction (θ) while leaved unmodified in the plane perpendicular to the incoming beam direction (ϕ). The energy deposited is expected to increase proportionally to $s \cdot \cos\theta$ (where s is the sensors thickness) is expected.

Fig. 45a shows the MPV value of the landau distribution fitting the cluster signal distribution as a function of the impact angle θ, while Fig. 45b shows the same values plotted as function of $\frac{1}{\cos\theta}$. MPV represents the energy loss of the incoming particle through the sensor, its value, measured in ADC, is here converted in energy using the linear calibration relation discussed in sec. 5.3.8.

The linear fit on Fig. 45b confirms the linearity dependence of the energy deposited on the length of the particles path through the sensor.

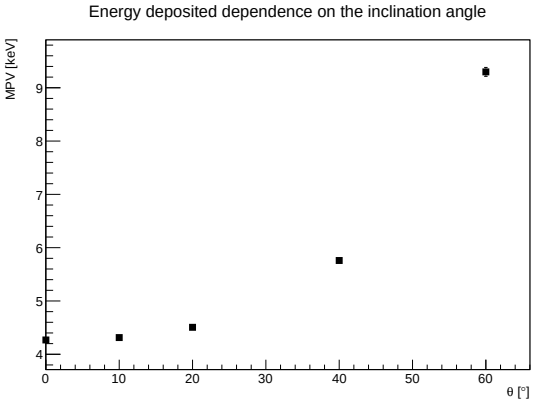

(a) MPV of the Cluster Signal distribution as a function of θ

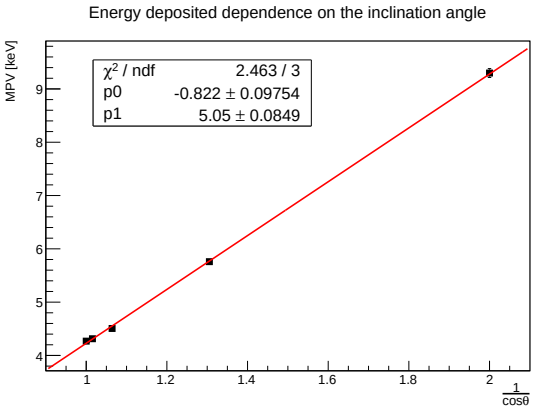

(b) MPV of the Cluster Signal distribution as a function of $\frac{1}{\cos\theta}$

Figure 45: MPV of the Cluster Signal distribution as a function of the azimuthal inclination angle (θ). The MPV values are expressed in keV using the energy calibration relation shown in sec. 5.3.8.